A Semi-Analytical Frequency Domain Model for Efficient Design Evaluation of Spar Floating Wind Turbines

John Marius Hegseth*, Erin E. Bachynski

NTNU, Department of Marine Technology, 7491 Trondheim, Norway

* Corresponding author. E-mail address: john.m.hegseth@ntnu.no

This research did not receive any specific grant from funding agencies in the public, commercial, or not-for-profit sectors.

Abstract

A linear model for efficient design evaluation of spar floating wind turbines is presented, and verified against a nonlinear time domain model with regards to long-term fatigue and short-term extreme response for two different spar designs. The model uses generalized displacements and a semi-analytical approach to establish the equations of motion for the system, which are solved in the frequency domain. The results show agreement within ± 30 % for the long-term fatigue considering operational conditions, however, the linear fatigue damage estimates are sensitive to the accuracy of the estimated natural frequency of the first bending mode. The results also suggest that a small number of environmental conditions can be simulated with a nonlinear time domain model to verify and possibly tune the linear model, which then can be used to run the full long-term analysis. Short-term extreme tower base bending moments and surge and pitch motions are observed to be nearly Gaussian above cut-out wind speed, as the response is dominated by wave forces. Consequently, the linear model is able to accurately capture the upcrossing rates, which are used to calculate the characteristic largest extreme response. For an operational case near rated wind speed, the response is somewhat non-Gaussian, which gives larger discrepancies between the linear and nonlinear models. However, due to large mean values in this condition, the total error in the extreme response is reduced, and reasonable agreement is achieved.

Keywords: offshore wind, design analysis, frequency domain, fatigue, extreme response

---

Nomenclature

α_2	Dirlik irregularity factor
β	Stiffness-proportional Rayleigh damping coefficient
Γ	Gamma function
ν_p	Expected rate of peaks
ρ	Water density
σ	Standard deviation
σ_x	Axial stress

ψ	Shape function
ω	Angular frequency
A	Cross sectional area
a	Hull radius
a_{11}	Transverse added mass per unit length
$\mathbf{B}$	Generalized damping matrix
B_{aero}	Aerodynamic damping
b_{visc}	Linearized viscous damping per unit length
C_d	Drag coefficient
D	Hull diameter
$\mathrm{d}F_W$	Wave excitation force per unit length
EI	Bending stiffness
$\mathbf{F}_\zeta$	Generalized wave load vector
F_T	Thrust force
$\mathbf{F}_U$	Generalized wind load vector
g	Gravitational acceleration
$\mathbf{H}_{ij}$	Transfer function from i to j
h	Water depth
I	Area moment of inertia
I_{RNA}	Inertia of the RNA about the tower top
I_{wp}	Waterplane area moment of inertia
J'_n	Derivative of Bessel function of the first kind of order n
$\mathbf{K}$	Generalized stiffness matrix
K	Material property for SN curve
K_r	Hydrostatic restoring in pitch
K_t	Linear horizontal mooring stiffness
k	Wave number, thickness exponent for SN curve
L	Spar FWT draft
$\mathbf{M}$	Generalized mass matrix
M	Mass of spar including mooring system
M_{RNA}	Mass of the RNA
M_T	Rotor moment

M_y	Bending moment about y-axis
m	Mass per unit length, slope of SN curve
m_n	n^{th} spectral moment
N	Axial force
r	Cross section outer radius
S_ζ	Wave spectrum
S_U	Wind spectrum
t	Wall thickness
t_{ref}	Reference thickness for SN curve
V	Hull displacement
x_m	Dirlik mean frequency
Y'_n	Derivative of Bessel function of the second kind of order n
z_B	Vertical centre of buoyancy
z_G	Vertical centre of gravity
z_{moor}	Vertical location of the fairleads
z_{TB}	Vertical location of the tower base
z_{top}	Vertical location of the tower top

1 Introduction

The offshore wind industry has had significant growth over the last decade, and as a majority of the global wind resources are located in deeper waters, there has recently been an increased interest in floating wind turbines (FWTs). For floating wind farms to be economically feasible, cost-effective and reliable designs are needed. Design optimization of FWTs is a complex task, and due to interactions between aerodynamics, hydrodynamics, structural dynamics and control, coupled nonlinear time domain (TD) simulations are usually applied. As numerous load cases need to be analysed, the design process becomes computationally very expensive. It is therefore desirable to use simplified models, especially in preliminary design [1]. Frequency domain (FD) models provide an efficient way of performing dynamic simulations and are frequently used for floating structures in the offshore industry, usually in fatigue analyses [2]. Although less common in the offshore wind industry, design standards state that frequency domain analyses also can be used to calculate the fatigue loads for FWTs, if validation against time domain analyses or experiments is performed [3].

Several studies have investigated the applicability of FD models for FWTs. Typically, these models have considered first order hydrodynamic loads from potential theory and steady aerodynamic loads, and have been used to calculate response amplitude operators (RAOs) for the rigid body motions of the platform [4–7].

Although useful information about the system may be found using only rigid body motions, the elasticity of the tower has been shown to significantly affect the global response of FWTs. Bachynski and Moan [8] compared a linear FD model with three rigid body modes to a nonlinear TD model for different tension leg platform wind turbine designs in both wave-only and combined wind-wave conditions. The study was later expanded to include turbulent wind excitation and aerodynamic damping [9], and concluded that the linear model was insufficient for design calculations, partly due to the rigid modelling of the tower. Kvittem and

Moan [10] used a similar procedure to calculate tower base bending moments for a semi-submersible wind turbine, where the first bending mode of the tower was found from a free decay test and included using generalized coordinates. The contribution from the first bending mode on the tower base bending moment response was expressed as a dynamic amplification factor. The model was found to perform reasonably well in the 13 considered load cases, however, the fatigue damage was underestimated by up to 60% due to its exponential nature. A somewhat different approach was applied by Kluger et al. [11], who used statistical linearization to develop a FD model for the OC3 spar wind turbine [12]. The two first elastic tower modes were found for a fixed foundation and included in the analysis, and equivalent fatigue stress (EFS) at the tower base due to wave excitation and steady wind was calculated for 11 different environmental conditions. The results were compared to values from TD simulations reported by Matha [13], where the FD analysis was found to underestimate the total EFS by 12%.

Although earlier work has assessed the fatigue damage based on FD analyses for FWTs, these calculations have only been performed for a limited number of environmental conditions. Thus, little information exists regarding the accuracy of such models for a full long-term analysis. In addition, the design process must also consider the extreme response of the system, which can be a comprehensive task. Results from previous studies have shown that both the tower base bending moment [14] and global motions [15] for spar FWTs can be quite Gaussian in harsh environmental conditions, which suggests that a linear model also may be used to assess the extreme response in early stages of design. For a spar FWT, in addition to the ultimate stresses in the structure, the extreme surge and pitch response of the platform may be of interest, as these motions are important for loads on the mooring system and nacelle components, respectively.

In the present work, a semi-analytical FD approach is presented, where generalized degrees-of-freedom (DOFs) are used to describe the dynamic behaviour of the FWT. The system is linearized, and due to the simple geometry of the hull, closed-form expressions may be used for the hydrodynamic loads with good accuracy. This removes the need for a separate numerical hydrodynamic analysis, which significantly increases the computational efficiency. The aerodynamic loads are found numerically from TD simulations, and the forces are superimposed to find the total response. The approach is then compared to fully coupled nonlinear TD simulations for two different 10 MW spar FWT designs, considering long-term fatigue damage at the tower base, as well as short-term extreme values for the tower base bending moment and surge and pitch motions of the platform in selected conditions along the 50-year environmental contour. The linear FD model presented in the present work is not applicable for detailed analyses, but may complement state-of-the-art tools in early stages of design. The model can help the designer get a quick overview of the response of the system, and give indications of how the system responds to changes in the design parameters. It may also be used to identify critical load cases, which then can be analysed using coupled nonlinear TD analyses.

2 System Description

2.1 Platform Designs

The two spar buoys considered in the current work are shown in Fig. 1. The designs are based on the OC3-Hywind design [12] and consist of two cylinders with different diameters, connected by a linearly tapered section. The hull extends to a height of 10 m above still water level (SWL), where it is fixed to the tower. Spar 1 has the same draft as the original OC3 spar of 120 m, but with increased diameters to provide enough buoyancy to support a 10 MW wind turbine, and to match the tower base diameter. The large draft of the spar provides good stability and hydrodynamic performance, however, it limits the use to deep water, and complicates construction and towing to site. The draft of the second design (spar 2) was therefore reduced by 25%, which makes it more suitable for intermediate water depths. In addition to the draft reduction, the lower hull diameter was increased by 25% compared to spar 1, to achieve a sufficient amount of buoyancy.

The two designs are presented in Table 1, where values for the vertical centre of gravity (CoG) and moment of inertia are calculated by assuming that the hulls are partially filled with concrete ballast to achieve the correct draft, using a ballast density of 2600 kg/m^3, while a constant wall thickness of 6 cm is assumed for the steel hull. The water depth for both platforms is 320 m.

Table 1: Platform properties.

Parameter	Spar 1	Spar 2
Draft (m)	120.0	90.0
Elevation to tower base above SWL (m)	10.0	10.0
Depth to top of taper below SWL (m)	4.0	4.0
Depth to bottom of taper below SWL (m)	12.0	12.0
Diameter above taper (m)	8.3	8.3
Diameter below taper (m)	12.0	15.0
Mass including ballast (kg)	1.18E+7	1.33E+7
Displacement (m^3)	1.31E+4	1.49E+4
Moment of inertia about CoG (kgm^2)	6.53E+9	3.42E+9
Vertical CoG below SWL (m)	94.7	72.3
Vertical CoB below SWL (m)	62.0	47.8

Table 2: Main characteristics of the DTU 10 MW reference wind turbine [16].

Parameter	Value
Rated power	10 MW
Rotor orientation and configuration	Upwind, three blades
Rotor, hub diameter	178.3 m, 5.6 m
Hub height	119.0 m
Cut-in, rated, cut-out wind speed	4.0 m/s, 11.4 m/s, 25.0 m/s
Cut-in, rated rotor speed	6.0 rpm, 9.6 rpm
Overhang, shaft tilt, pre-cone	7.1 m, 5.0°, -2.5°
Rotor, nacelle, tower mass[1]	230.7 t, 446.0 t, 628.4 t

[1] Mass for original land-based tower.

2.2 DTU 10 MW Wind Turbine with Modified Tower

The spar buoys support the DTU 10 MW reference wind turbine [16], with the tower shortened by 10 m to achieve the same hub height as the onshore turbine at 119 m above SWL. The tower has a linearly tapered outer diameter and consists of ten sections with constant wall thickness in each section. In the modified tower, each section is shortened by 1 m, while the top and bottom diameters are kept unchanged. The key characteristics of the turbine are listed in Table 2.

The natural frequencies of the tower change when the turbine is placed on a floating substructure, and preliminary calculations showed that the natural frequency of the first bending mode for spar 2 was very close to the blade passing frequency at rated rotor speed. The wall thickness in all sections of the tower was therefore increased by 50% for spar 2, which moved the natural frequency above the 3P range.

2.3 Mooring System

The mooring system, described in Table 3, consists of three catenary lines spread symmetrically about the vertical axis. As in the OC3 project, a simplification is made in that the delta lines are removed, and lines with constant properties are instead used all the way up to the fairleads. A rotational spring is added to

Table 3: Mooring system properties.

Parameter	Spar 1	Spar 2
Radius to anchors (m)	855.2	855.2
Unstretched mooring line length (m)	902.2	902.2
Equivalent mooring line mass density (kg/m)	155.4	155.4
Equivalent mooring line axial stiffness (MN)	3.84E+8	3.84E+8
Fairlead depth below SWL (m)	77.2	56.3
Yaw spring stiffness (Nm/rad)	1.48E+8	1.48E+8

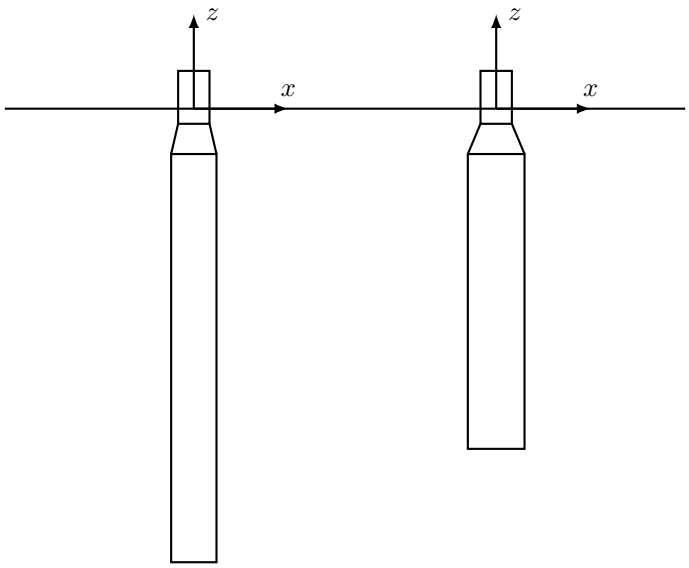

Figure 1: Spar designs considered in the present work. Spar 1 (left) and spar 2 (right).

the model to ensure that the yaw stiffness from the mooring system is included. The fairleads are placed at a depth equal to the total CoG of the system including the wind turbine, in order to limit the coupling between surge and pitch motion. This results in a slightly stiffer mooring system for spar 2.

3 Time Domain Model

The fully coupled nonlinear aero-hydro-servo-elastic analyses are carried out in the time domain using the simulation workbench SIMA developed by SINTEF Ocean, which couples two computer codes: Riflex, a finite element solver developed for flexible beam elements; and SIMO, which calculates large volume hydrodynamic loads [17, 18]. The spar buoys are modelled as six-DOF rigid bodies with first order wave forces found numerically from potential flow theory using WAMIT [19], combined with viscous forces from the drag term in Morison's equation, which are integated up to the instantaneous wave elevation. Second order potential flow forces are not considered in the model, as studies have shown that these loads have limited effect on the response for spar-type FWTs [20, 21].

Bar elements with only axial stiffness are used to model the mooring lines, together with hydrodynamic loads from Morison's equation. The model thus includes the nonlinear restoring forces from the mooring system, as well as the dynamic behaviour of the mooring lines. The tower and blades are modelled using flexible beam elements.

The aerodynamic loads are calculated using blade element/momentum (BEM) theory, including Glauert correction, Prandtl hub and tip loss factors, dynamic stall, dynamic wake, skewed inflow and tower shadow. The code has previously been verified for FWTs [22, 23]. As wind drag forces on the tower may become important at high wind speeds, this effect is included for the extreme response conditions using a drag force formulation with a drag coefficient of 0.7.

An external control system written in Java is used to modify the generator torque and blade pitch. In order to avoid pitch motion instability above rated wind speed due to negative feedback [24, 25], the proportional and integral gains for the blade pitch are modified from the original controller. With the resulting gains, the controller has a natural frequency of 0.13 rad/s and a damping ratio of 0.7.

4 Frequency Domain Model

In the frequency domain model, a linear representation of the system is created as shown in Fig. 2. For simplicity, only the response in the xz-plane is considered in the present study. The platform is considered rigid, while the tower is modelled as a slender flexible beam. The rotor and nacelle assembly (RNA) is replaced by a point mass and inertia at the top of the tower, with resultant wind loads (thrust force, rotor pitching moment, and aerodynamic damping) acting on the tower top. The mooring system is represented by a linear spring at the position of the fairleads. As the structure is statically determinate, internal loads in the hull can be found by considering equilibrium between external, inertial, damping and internal reaction forces. In the present work, the tower base bending moment is the only internal load which is considered (see also Appendix A), but the method can easily be applied to other components.

Generalized displacements are used in combination with the principle of virtual work to establish the dynamic equations of motion [26], which are solved in the FD. In this procedure, the total response is described by a weighted combination of an arbitrary number of shape functions, ψ. The accuracy of the formulation thus depends on how well the actual displacement field is captured by the shape functions, which typically are chosen to represent the most important eigenmodes of the system.

Three generalized DOFs are included in the model, namely surge, pitch, and the first bending mode, as illustrated in Fig. 3. Orthogonal eigenmodes can be found numerically from the solution of the eigenvalue problem for a finite element (FE) model of the linearized system. However, as the shapes of the rigid body modes are known a priori, they are instead chosen as analytical functions for simplicity. In addition, to have global motions that are consistent with the TD model, the pitch mode is chosen as a rotation about the SWL. Using non-orthogonal modes introduces off-diagonal terms in the system matrices, however, these coupling effects are readily taken into account in the formulation.

The actual shape of the bending mode, on the other hand, is not known, and is therefore found from the eigenvalue solution. A third-order spline function is then fitted to the nodal displacements to have continuous expressions for the first and second order derivatives. The FE model used to solve the eigenvalue problem is based on the linearized system in Fig. 2 and does not include the blades, however, added mass on the hull is included using strip theory.

4.1 Load Formulation

In order to predict the dynamic behaviour of the system, the inertia, damping, restoring and excitation forces on the structure need to be determined. Due to the simple and relatively slender geometry of the hull, the hydrodynamic loads on the floater can be simplified without significant loss of accuracy. The transverse added mass per unit length is approximated using the analytical expression for a 2D circular cylinder with diameter D in infinite fluid [27]:

$$a_{11}(z) = \rho\pi D^2(z)/4 \tag{1}$$

The linear wave excitation forces are taken from MacCamy-Fuchs theory [28]. The force per unit length, $\mathrm{d}F_W$, for a regular wave with unit amplitude is given by

$$\mathrm{d}F_W(z,\omega) = \frac{4\rho g}{k}\frac{\cosh k(z+h)}{\cosh kh}\, G\, e^{i(\omega t-\alpha)} \tag{2}$$

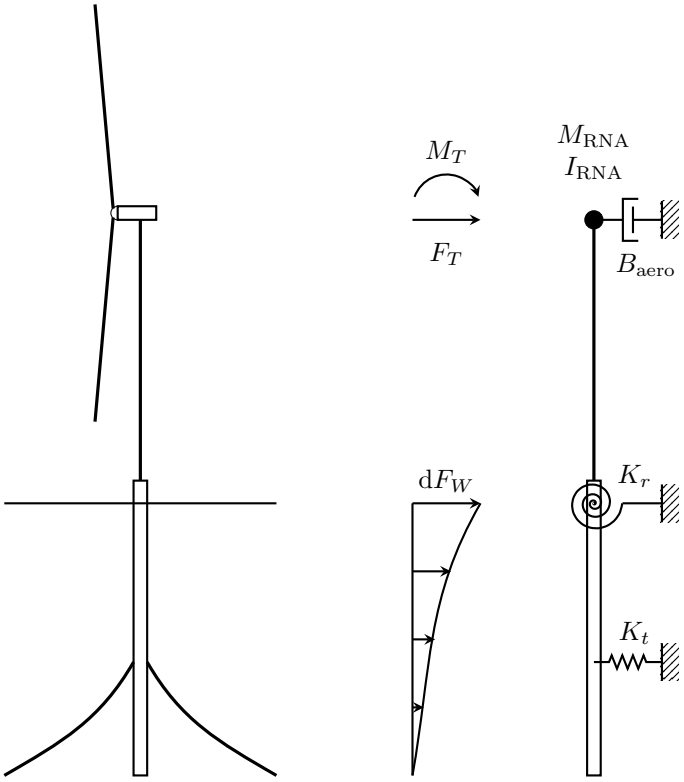

Figure 2: Linear representation of the FWT system.

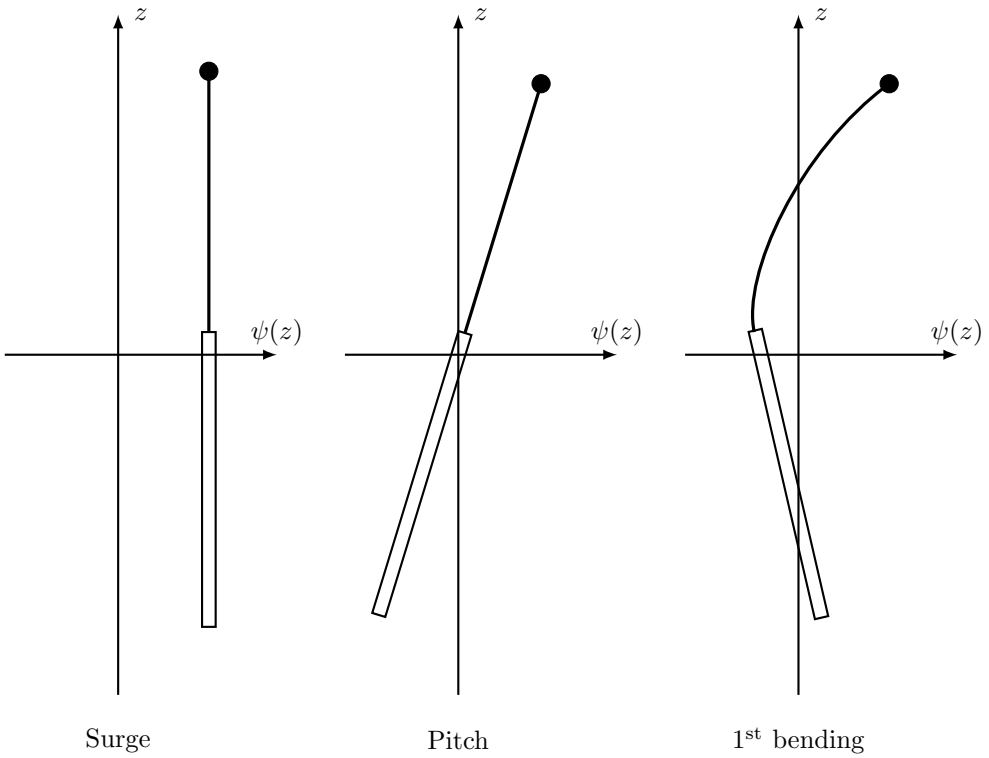

Figure 3: DOFs considered in the analysis.

where

$$G = \frac{1}{\sqrt{\left(J_1'(ka)\right)^2 + \left(Y_1'(ka)\right)^2}}, \quad \tan\alpha = \frac{J_1'(ka)}{Y_1'(ka)}. \tag{3}$$

For the aerodynamic loads, the BEM equations usually have to be solved in the TD [29], and there is no straight-forward way to establish linearized frequency-dependent wind forces. In the present study, the turbulent thrust force (F_T) and rotor moment (M_T) for different wind speeds are extracted from TD simulations on a fixed rotor in SIMA. The resulting time series are transformed to the FD using fast Fourier transform (FFT), and normalized with the incoming wind spectrum to create force transfer functions. In addition, the so-called aerodynamic damping, which arises due to the change in thrust force as a result of the nacelle's velocity, needs to be explicitly calculated, which can be done in various ways [29, 30]. Here, the linearized damping is estimated following the procedure described by Bachynski [9]. Time domain simulations with a range of constant wind speeds are run on a fixed rotor, and the damping values are found as the change in thrust force for small variations in wind speed while the blade pitch and rotor speed are kept fixed:

$$B_{\text{aero}} = \frac{\mathrm{d}F_T}{\mathrm{d}U}. \tag{4}$$

The resulting aerodynamic damping values are shown as a function of mean wind speed in Fig. 4, presented as critical damping ratio for the first fore-aft tower mode of the original land-based DTU 10 MW turbine. The linearized aerodynamic damping applies to all generalized modes with nonzero deflection at the tower top, and the coefficient B_{aero} is varied with the mean wind speed. Damping caused by pure rotation of the rotor is not considered. It is assumed that any changes in aerodynamic forces that arise due to the motions of the FWT are captured by the aerodynamic damping term, which means that variations in control system outputs caused by platform motions are not considered in the model.

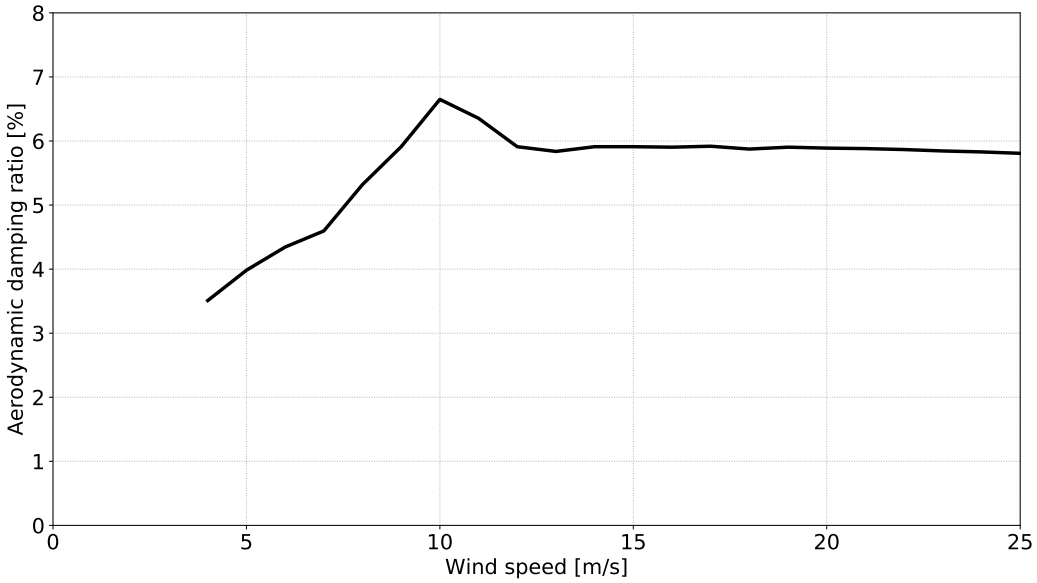

Figure 4: Aerodynamic damping ratio for the first fore-aft mode of the land-based DTU 10 MW turbine as a function of wind speed.

Rayleigh damping is used to model structural damping in the tower, with a stiffness-proportional coefficient $\beta = 0.007$ for both designs. For a given β, the damping ratio is proportional to the natural frequency, and using a constant value will thus reward stiffer designs, such as spar 2, without any physical reason. In an actual design process, the coefficient should therefore be continuously updated to keep the damping ratio constant. However, as the scope of the current work is not to perform design calculations, but rather to compare different modelling techniques, a constant coefficient is used for simplicity. The applied coefficient corresponds to a damping ratio of 0.9% and 1.2% at the first bending natural frequency for spar 1 and spar 2, respectively.

Viscous damping, which is important for the low-frequency surge response, is added based on stochastic linearization of the quadratic drag term in Morison's equation [31]:

$$\frac{1}{2}\rho C_d D(z)\dot{x}|\dot{x}| \approx \frac{1}{2}\rho C_d D(z)\sqrt{\frac{8}{\pi}}\sigma_{(\dot{x})}(z)\dot{x} = b_{\text{visc}}(z)\,\dot{x} \tag{5}$$

with a drag coefficient $C_d = 0.7$. The standard deviation of the velocity, $\sigma_{(\dot{x})}$, is found using an iteration scheme. Viscous wave excitation was found to be small compared to the wind excitation forces, and is therefore not included in the model. Wave radiation damping is also neglected. The aerodynamic drag forces on the tower, which only are included in the extreme response conditions, is taken into account in the linear model as a combination of a mean force, which is added directly, and a frequency-dependent force, which is found using stochastic linearization. Here, only the excitation forces are considered, meaning that the tower drag forces arising from the movement of the turbine are neglected.

The analytical solution for quasi-static horizontal tension in elastic catenary lines can be found in e.g. Faltinsen [32]. In order to find the linear mooring stiffness used in the model, K_t, this equation is differentiated numerically. The stiffness is calculated for the zero offset position of the hull in all environmental conditions, as the offset was found to have little effect on the results. However, updated stiffness values based on the actual mean position of the platform can easily be included. Mooring line excitation, damping and inertia are neglected in the model.

The hydrostatic restoring in pitch, which is applied as a rotational spring at the SWL, is found from

$$K_r = \rho g V z_B - M g z_G + \rho g I_{\text{wp}}. \tag{6}$$

4.2 Establishing the Equations of Motion

Using the vector containing the shape functions and the terms derived in the previous section, the generalized mass (including added mass), damping and stiffness matrices can be established [26]:

$$\begin{aligned}\mathbf{M} = &\int_0^{z_{\text{top}}} m(z)\boldsymbol{\psi}(z)\boldsymbol{\psi}^\top(z)\mathrm{d}z + \int_{-L}^{0}[m(z)+a_{11}(z)]\boldsymbol{\psi}(z)\boldsymbol{\psi}^\top(z)\mathrm{d}z \\ &+ M_{\text{RNA}}\boldsymbol{\psi}(z_{\text{top}})\boldsymbol{\psi}^\top(z_{\text{top}}) + I_{\text{RNA}}\boldsymbol{\psi}_{,\boldsymbol{z}}(z_{\text{top}})\boldsymbol{\psi}_{,\boldsymbol{z}}{}^\top(z_{\text{top}})\end{aligned} \tag{7}$$

$$\mathbf{B} = \beta\int_{z_{\text{TB}}}^{z_{\text{top}}} EI(z)\boldsymbol{\psi}_{,\boldsymbol{zz}}(z)\boldsymbol{\psi}_{,\boldsymbol{zz}}{}^\top(z)\mathrm{d}z + \int_{-L}^{0} b_{\text{visc}}(z)\boldsymbol{\psi}(z)\boldsymbol{\psi}^\top(z)\mathrm{d}z + B_{\text{aero}}\boldsymbol{\psi}(z_{\text{top}})\boldsymbol{\psi}^\top(z_{\text{top}}) \tag{8}$$

$$\begin{aligned}\mathbf{K} = &\int_{z_{\text{TB}}}^{z_{\text{top}}} EI(z)\boldsymbol{\psi}_{,\boldsymbol{zz}}(z)\boldsymbol{\psi}_{,\boldsymbol{zz}}{}^\top(z)\mathrm{d}z + \int_{z_{\text{TB}}}^{z_{\text{top}}} N(z)\boldsymbol{\psi}_{,\boldsymbol{z}}(z)\boldsymbol{\psi}_{,\boldsymbol{z}}{}^\top(z)\mathrm{d}z \\ &+ K_t\boldsymbol{\psi}(z_{\text{moor}})\boldsymbol{\psi}^\top(z_{\text{moor}}) + K_r\boldsymbol{\psi}_{,\boldsymbol{z}}(0)\boldsymbol{\psi}_{,\boldsymbol{z}}{}^\top(0),\end{aligned} \tag{9}$$

where $N(z)$ is the axial force in the tower. The generalized wind and wave load vectors are found from

$$\mathbf{F}_U(\omega) = F_T(\omega)\boldsymbol{\psi}(z_{\text{top}}) + M_T(\omega)\boldsymbol{\psi}_{,\boldsymbol{z}}(z_{\text{top}}) \tag{10}$$

$$\mathbf{F}_\zeta(\omega) = \int_{-L}^{0} dF_W(z,\omega)\boldsymbol{\psi}(z)\mathrm{d}z. \tag{11}$$

4.3 Frequency Domain Response

The transfer functions relating modal response to wave and wind input, $\mathbf{H}_{\zeta X}(\omega)$ and $\mathbf{H}_{UX}(\omega)$ respectively, are defined as

$$\mathbf{H}_{\zeta X}(\omega) = \mathbf{H}_{FX}(\omega)\mathbf{F}_\zeta(\omega),\ \mathbf{H}_{UX}(\omega) = \mathbf{H}_{FX}(\omega)\mathbf{F}_U(\omega) \tag{12}$$

where

$$\mathbf{H}_{FX}(\omega) = \left[-\omega^2\mathbf{M} + i\omega\mathbf{B} + \mathbf{K}\right]^{-1} \tag{13}$$

is the frequency response function matrix. Transfer functions between tower base bending moment and wind/wave input ($H_{\zeta M}(\omega)$ and $H_{UM}(\omega)$) are found by considering equilibrium between external, inertial, damping and internal forces. The complete equations may be found in Appendix A. As both the wind speed and wave elevation are considered to be stationary Gaussian processes within the short-term duration, the linear response will also be a stationary Gaussian process. The responses to wind and wave input are assumed to be independent; that is, there is no interaction between the responses at different frequencies. This is an assumption inherent in the linearization, and may not be equally applicable for all FWTs.

The response spectrum for an arbitrary response parameter ξ is then found by superimposing the wind and wave responses:

$$S_\xi(\omega) = |H_{\zeta\xi}(\omega)|^2 S_\zeta(\omega) + |H_{U\xi}(\omega)|^2 S_U(\omega), \tag{14}$$

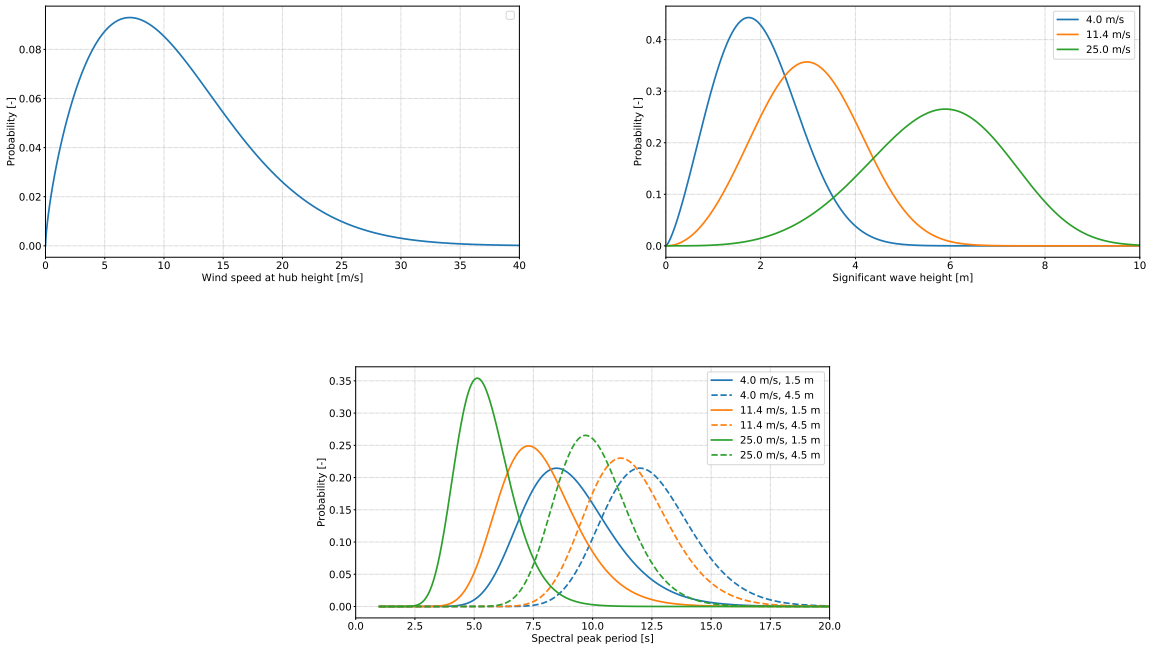

Figure 5: Marginal distribution of 1-h wind speed, and conditional distributions of wave height and peak period. Based on Johannessen et al. [33].

while the variance is given as

$$\sigma^2_{(\xi)} = \int_0^\infty S_\xi(\omega)\,\mathrm{d}\omega. \tag{15}$$

5 Dynamic Simulations

5.1 Environmental Conditions

The long-term fatigue assessment uses the joint probability distribution of metocean parameters given in Johannessen et al. [33]. Probability density functions (PDFs) for the parameters are shown in Fig. 5. IEC 61400-3 [34] prescribes a minimum bin size of 2 m/s for the wind speed, 0.5 m for wave heights, and 0.5 s for wave periods. Kvittem and Moan [35] performed a long-term fatigue analysis of a semi-submersible FWT, where damage sensitivity with regards to simulation length, bin size and number of samples were addressed. Based on their findings, the bin size for wave heights and wave periods in the present work are increased to 1 m and 1 s, respectively, and each condition is simulated using six 1-h realizations after removal of transients.

Long-term fatigue analyses used in design of FWTs should cover all relevant conditions over the lifetime of the structure, including operational, fault, idling, and survival conditions. The fatigue analysis presented in this study is limited to operational cases, which means that the mean wind speed is varied between 4 and 25 m/s, and the turbine is assumed to be operating normally. A total of 546 environmental conditions (ECs) are thus considered in the analysis, which corresponds to all ECs within 4-25 m/s with probability of occurrence greater than 10^{-4}. It is worth noting that, although not employed in the current fatigue comparison, the FD model also is applicable for wind speeds below cut-in or above cut-out, as long as only steady-state conditions are considered.

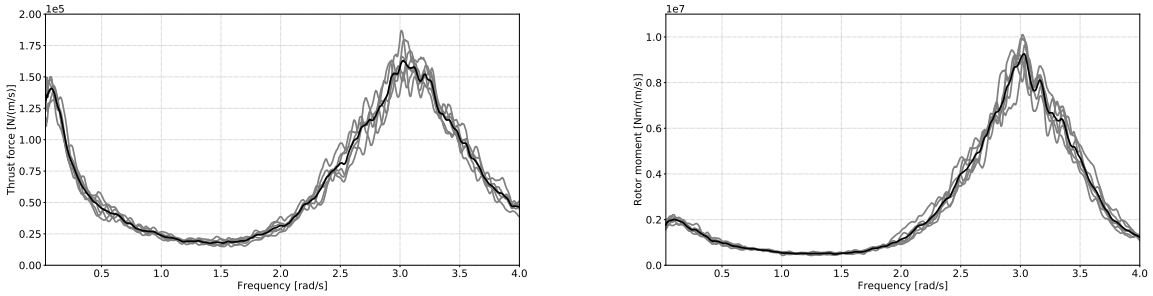

Figure 6: Calculated transfer functions for aerodynamic excitation loads at 11 m/s mean wind speed. Six different wind realizations (grey) and average values (black).

Table 4: Environmental conditions for extreme response calculation.

Condition	1	2	3	4
Mean wind speed at hub height, U (m/s)	11.0	25.0	36.0	50.0
Significant wave height, H_s (m)	6.9	10.3	12.9	15.1
Spectral peak period, T_p (s)	10.0	12.5	14.0	16.0
Turbulence intensity at hub height, I (-)	0.18	0.14	0.13	0.12

Three-dimensional turbulent wind time series are generated using TurbSim [36], assuming a Kaimal spectrum for IEC61400-1 class B turbines and a normal turbulence model. A power law profile with exponent 0.14 is used to model the vertical wind shear [34]. The same wind files are used both directly in the TD simulations, and to establish the wind thrust and rotor moment transfer functions used in the FD calculations, which are derived by taking the average values over the six seeds. The calculated transfer functions for each individual wind time series, as well as the average curves, are shown in Fig. 6 for 11 m/s mean wind speed, to illustrate the degree of variability between the realizations. Wave time series are generated using JONSWAP spectra with a peakedness parameter of 3.3. Co-directional waves and wind travelling in the positive x-direction are applied in all simulations, and no current is considered in the analysis.

Four ECs along the 50-year contour surface are selected to compare the short-term extreme response, as described in Table 4. In EC 1, the mean wind speed is close to the rated speed of the turbine, which gives the maximum thrust force on the rotor. EC 2 considers an operational condition near cut-out, while ECs 3 and 4 represent wind speeds above cut-out, where the turbine is parked and the blades are feathered. As for the fatigue analysis, 1-h simulations (excluding transients) are used in the extreme response comparison, but with 20 different random seeds for each condition. No fault conditions are considered, however, previous studies on blade pitch faults, grid loss and shutdown have shown that such events primarily affect the loads on the blades and shaft, and that the tower base fore-aft bending moment and global motions tend to be smaller than during fault-free conditions for spar-type FWTs [37, 38].

5.2 Fatigue Damage Assessment

The fore-aft axial stress at the outer radius of the tower is calculated from

$$\sigma_x = \frac{N}{A} + \frac{M_y}{I}\, r. \tag{16}$$

Stress variations due to fluctuations in the axial force are found to be negligible compared to the moment-induced stress variations, and are thus not included in the fatigue calculations. In the TD, rainflow counting

is used together with SN curves and the Miner-Palmgren rule to estimate the fatigue damage, which is taken as the average value over the six realizations for each EC. In the FD, two different methods are considered:

1. Inverse Fourier transform (IFT)
2. Dirlik method

In the first method, 1-h stress time series are generated by performing IFT on the response spectrum with random phase angles. The fatigue damage is then calculated using rainflow counting and the Miner-Palmgren rule. The phase angles will introduce randomness to the damage estimates, and the method is therefore performed with six different random seeds, as for the TD model. The average value is then used in the fatigue comparison.

The Dirlik method [39] uses the stress response spectrum and empirical factors to fit the PDF of the stress cycles to a combination of an exponential and two Rayleigh distributions, and the accuracy of the method is therefore dependent on how well the rainflow-count can be represented by these distributions. The expression for the fatigue damage during T seconds becomes [26]:

$$D_{\mathrm{DK}} = \frac{\nu_p T}{K}(2\sigma)^m \left(G_1 Q^m \Gamma(1+m) + (\sqrt{2})^m (G_2 R^m + G_3)\Gamma(1+\frac{m}{2}) \right) \left(\frac{t}{t_{\mathrm{ref}}} \right)^{mk} \tag{17}$$

where

$$\begin{gathered} G_1 = \frac{2(x_m - \alpha_2^2)}{1+\alpha_2^2},\ G_2 = \frac{1-\alpha_2-G_1+G_1^2}{1-R}, \\ G_3 = 1 - G_1 - G_2,\ Q = \frac{1.25(\alpha_2 - G_3 - G_2 R)}{G_1}, \\ R = \frac{\alpha_2 - x_m - G_1^2}{1-\alpha_2-G_1+G_1^2} \end{gathered} \tag{18}$$

and

$$\begin{gathered} \alpha_2 = \frac{m_2}{\sqrt{m_0 m_4}},\ x_m = \frac{m_1}{m_0}\sqrt{\frac{m_2}{m_4}}, \\ \nu_p = \frac{1}{2\pi}\sqrt{\frac{m_4}{m_2}}. \end{gathered} \tag{19}$$

Here, m_n is the n^{th} spectral moment, defined as:

$$m_n = \int_0^\infty \omega^n S(\omega) \mathrm{d}\omega. \tag{20}$$

The Dirlik method has previously been shown to give accurate results over a wide range of bandwidths for a stationary Gaussian process [40], and the closed-form expression makes it well-suited for efficient design optimization. However, the accuracy of the method deteriorates if the fatigue loads are dominated by a few frequency components [41].

The SN curve used for the tower base is the D curve in air taken from DNV-RP-C203 [42]. The curve is bilinear, i.e. the material parameters, and thus also the slope of the curve, change at a certain stress range. For the rainflow procedure, this is easily taken into account, however, the Dirlik method only allows for single-slope curves. Based on initial calculations, the Dirlik damage estimation is performed with material parameters valid for stress ranges above 52.63 MPa (fewer than 10^7 cycles).

5.3 Short-term Extreme Response

Several methods have been used to estimate the short-term extreme response of FWTs, such as the Gumbel method and Weibull tail method for global motions [15, 43], and the Winterstein method for the tower base bending moment [14]. The present study uses the average upcrossing rate (AUR) method, see e.g. Naess

and Gaidai [44], which previously has been shown to perform well for a bottom-fixed offshore wind turbine under combined wind and wave loading [45]. The AUR method is based on the assumption that upcrossings of high levels are statistically independent, which means that the number of upcrossings during time T will be Poisson distributed. The cumulative distribution function (CDF) of the extreme value Y may thus be written as

$$F_Y(y) = \exp\left\{-\nu^+(y)\,T\right\}, \tag{21}$$

where Y can represent an arbitrary response parameter, such as tower base bending moment, global motions of the platform, or mooring line tension. $\nu^+(y)$ is the mean upcrossing rate of level y, which can be estimated empirically from j simulated time series of length T_0:

$$\hat{\nu}^+(y) = \frac{1}{jT_0}\sum_{i=1}^{j} n_i^+(y;T_0) \tag{22}$$

where $n_i^+(y;T_0)$ is the number of upcrossings in time series i. Assuming that the appropriate asymptotic extreme value distribution for the considered response is the Gumbel distribution, the tail of the mean upcrossing rate may be written as

$$\nu^+(y) = q(y)\exp\left\{-a(y-b)^c\right\},\ y \geq y_0 \tag{23}$$

where $q(y)$ is slowly varying and can be approximated as a constant. The parameters a, b, c and q are then determined by fitting Eq. (23) to the empirical data, as described in detail by Saha and Naess [46]. This is done by minimizing the mean square error function:

$$F(a,b,c,q) = \sum_{i=1}^{N} w_i\ \left|\ln\hat{\nu}^+(y) - \ln q + a(y_i-b)^c\right|^2 \tag{24}$$

using the Levenberg-Marquardt least-squares optimization algorithm. w_i is a weight factor which puts more emphasis on the more reliable data points, and is found from the estimated 95% confidence interval.

The AUR method is also applicable for the linear model, where an analytical expression is available. For a stationary Gaussian process with zero mean, the upcrossing rate can be written as [26]:

$$\nu^+(y) = \nu^+(0)\exp\left\{-\frac{y^2}{2\sigma^2}\right\}, \tag{25}$$

where $\nu^+(0)$ is the mean zero-upcrossing rate, which can be found from the zeroth and second order spectral moments:

$$\nu^+(0) = \frac{1}{2\pi}\sqrt{\frac{m_2}{m_0}}. \tag{26}$$

The characteristic largest extreme response y_{1h}, i.e. the most probable maximum value in one hour, is used to compare the TD and FD models. The value is found approximately from the following relation:

$$F_Y(y_{1h}) = \mathrm{e}^{-1}. \tag{27}$$

6 Results

6.1 Natural Periods

The natural periods of the linear system are estimated and compared to results from decay tests performed with the TD model in still water, as shown in Table 5. The decay tests are performed by releasing the platform from an offset position in the considered DOF, and the natural period is then found from the decaying motion. For the first bending mode, the hull is released together with the tower top, such that the coupling between platform pitch and tower bending is included.

Table 5: Natural periods.

Mode	Spar 1		Spar 2	
	TD	FD	TD	FD
Surge (s)	120.55	122.22	116.80	121.67
Pitch (s)	35.48	36.39	38.29	39.81
1st bending (s)	2.41	2.42	1.79	1.85

The FD model slightly overestimates the natural periods, which for the rigid modes is found to mainly be a consequence of the simplified added mass formulation. The reason why the first bending natural frequency is better approximated for spar 1 than spar 2 can be understood by examining the eigenmodes. In Fig. 7, the bending mode from the linearized eigenvalue solution is compared to the mode shape found from a decay test in TD, where a bandpass filter around the natural frequency is used to extract the shape including one of the blades. Due to the increased stiffness of the tower in spar 2, the coupled blade-tower mode changes, and the blades undergo a larger amount of bending. The simplification of replacing the RNA by a point mass and inertia is thus less accurate than for spar 1, where the blades behave more like a rigid body in the first tower bending mode. The shape of the tower is, however, seemingly not affected by the blade behaviour, and both designs show good agreement between the decay tests and the eigenvalue solutions.

6.2 Fatigue Damage

6.2.1 Linear and Nonlinear Estimates

Weighted 1-h fatigue damage is shown as a function of wind speed in Fig. 8. The linear predictions are seen to agree well with the TD results for spar 1, especially at wind speeds from 11 m/s and higher. For spar 2, the linear model is seen to overpredict the fatigue damage quite consistently by about 25-35%. The reasons for this overprediction are further explored in Section 6.2.2. The good agreement for spar 1 can be explained by the fact that that the tower base bending moment is close to Gaussian in most of the considered environmental conditions, in particular at higher wind speeds, which are associated with larger waves. The response in these conditions is dominated by wave forces and by resonant motions, which tend to be Gaussian even for non-Gaussian loads [47].

A notable difference between the linear and nonlinear results for spar 1 is seen at 9 m/s, where the 3P frequency is very close to the natural frequency of the first bending mode, which leads to resonance and thus a significant increase in fatigue damage for the FD model. In TD, the resonance has a rather limited effect on the damage estimates, possibly due to nonlinearities in the model.

With a few exceptions, the IFT and Dirlik results agree well for all conditions in both designs. Compared to the TD model, the error in total fatigue damage is 10.6% (IFT) and 7.1% (Dirlik) for spar 1, and 30.4% (IFT) and 30.9% (Dirlik) for spar 2.

Scatter plots showing the calculated fatigue damage for each environmental condition in TD and FD are presented in Fig. 9, where the Dirlik results are used for the linear model. The solid black line indicates perfect agreement, while conservative FD predictions are found below the line.

The accuracy of the linear model is to a large extent insensitive to the amount of fatigue damage in the individual conditions, and the data follow a fairly straight line, with most points located within ± 10% of the line of best fit for both designs. For spar 1, this line, when neglecting the 9 m/s conditions, is very close to the diagonal. The 9 m/s results, although being highly overestimated by the linear model, are also seen to be reasonably consistent, as the ratio between the linear and nonlinear estimates is more or less constant with increasing damage.

For spar 2, all points are located below the 1:1 line, and as for spar 1, the conditions with the largest discrepancies between linear and nonlinear predictions are in general found at lower wind speeds (5-9 m/s). These wind speeds are associated with low sea states, and little excitation of the bending mode. The

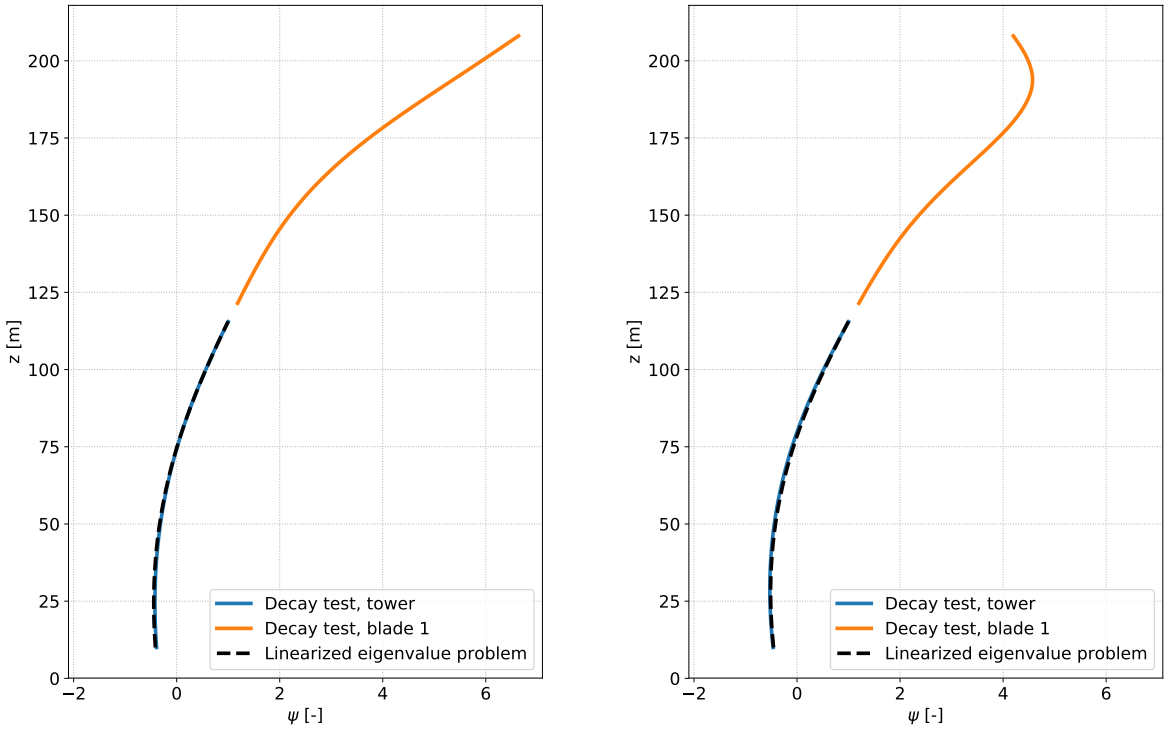

(a) Spar 1 **(b)** Spar 2

Figure 7: Normalized bending mode shapes.

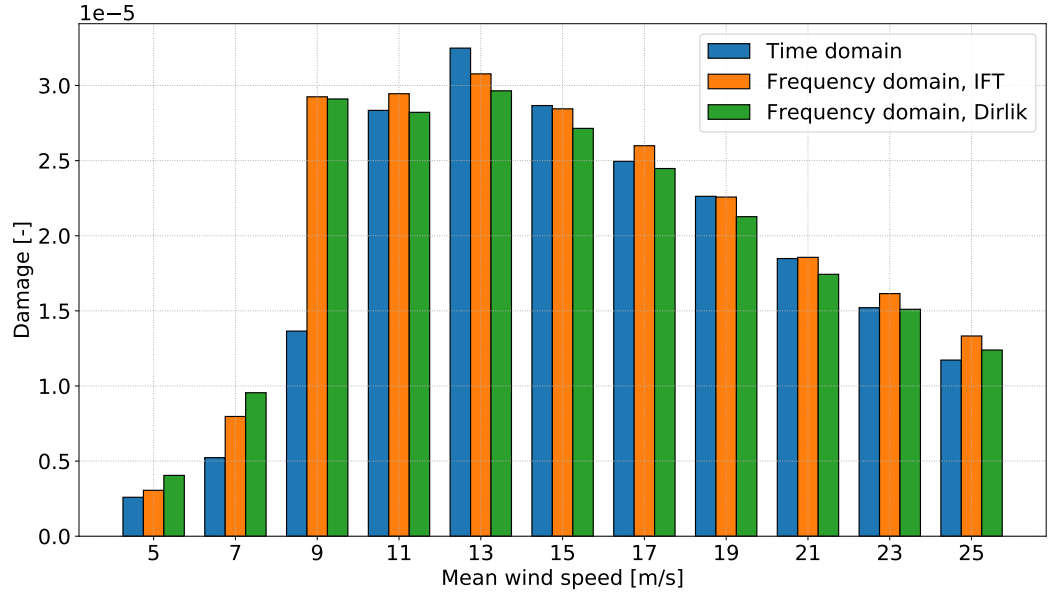

(a) Spar 1.

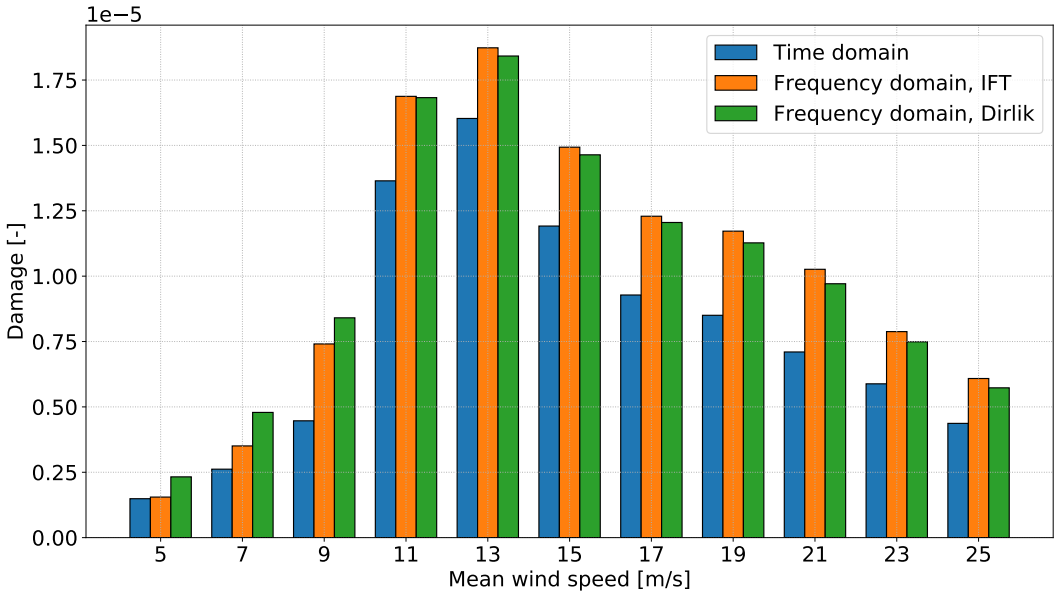

(b) Spar 2.

Figure 8: 1-h weighted fatigue damage arranged by wind speed.

tower base bending moment is thus dominated by the low-frequency wind response, which is less accurately predicted by the linear model than the wave- and bending-frequency response. The low-frequency response in the linear model is also somewhat sensitive to how the thrust force spectrum is estimated, as reported by Kvittem and Moan [10]. It should be noted that these conditions are associated with relatively small bending moments, and their contribution to the total fatigue damage over the lifetime of the structure is thus not significant.

The limited scatter in the data for both designs suggest that it is possible to simulate a small number of environmental conditions in the TD to verify and, if necessary, calibrate a linear model which can be used to perform the full long-term analysis. The verification cases should cover the entire wind speed range, as resonance effects may have a large impact on the accuracy of the model. In addition, a 1 m/s interval for the wind speed bins may be needed to correctly capture the response around possible resonance wind speeds [35].

6.2.2 Sensitivity to Errors in Natural Frequency

From the tower base stress spectra in Fig. 10, the reason for the general overprediction in fatigue damage by the linear model for spar 2 is obvious: the response in the region of the first bending mode is captured quite well by the linear model for spar 1, but is significantly overestimated for spar 2. The wave-frequency response is accurately estimated for both designs, whereas the low-frequency response is underpredicted at the pitch resonance frequency, mainly due to interaction between platform motion and the wind turbine controller in the TD model. Due to the limited number of cycles, however, the low-frequency response has little influence on the fatigue damage in the tower compared to the wave- and bending-frequency responses.

The overestimation of the response around the natural frequency of the first bending mode originates mainly from the small error in estimated natural period for the bending mode discussed in Section 6.1, as the wind excitation loads vary significantly with frequency in this region. In Fig. 11, the natural frequencies found from FD and TD are shown together with the transfer functions for thrust force and rotor moment at 21 m/s mean wind speed. From the figure, one clearly sees that the loads are reduced when the natural frequency for spar 2 is increased. The effect is most prominent for the rotor moment, which is about 25% lower at the TD natural frequency than at the natural frequency found from the linearized eigenvalue solution. To quantify the importance of this error on the fatigue damage results, the natural period of the bending mode is shifted from 1.85 s to 1.79 s in the linear model by adding an artificial stiffness term, and the fatigue analysis is rerun. The results, presented in Fig. 12, show a large improvement at most wind speeds, and the total fatigue damage error is reduced by approximately 50%. This highlights the importance of having accurate estimates for the natural frequency and shape of the first bending mode, which is dependent on how well the RNA can be approximated as a rigid body. In an optimization process, the accuracy of the model simplification may vary as changes are made to the design, however, this can be taken into account by a straightforward calibration of the natural frequency in the linear model.

The eigenmode in tower bending depends on wind speed, due to increased blade stiffness caused by centrifugal forces and pitching of the blades, as well as changes in the mean platform pitch angle. This is illustrated in Fig. 13, where mode shapes from decay tests are shown for calm air and 21 m/s uniform wind. As a consequence, the natural frequency of the bending mode is slightly increased by 2-3% at higher wind speeds. In addition, the mode shape derivative at the tower top is reduced by up to 20%.

From Fig. 11, an increase in the natural frequency of the bending mode is seen to result in higher wind loads for spar 1. However, this effect is counteracted by the decrease in the tower top derivative, which reduces the generalized wind load caused by the rotor moment (see Eq. (10)). For spar 2, on the other hand, both effects reduce the wind excitation loads for the bending mode, and cause the tuned linear model to somewhat overestimate the fatigue damage at higher wind speeds, as observed in Fig. 12.

Regarding the bending-frequency response, it should also be mentioned that, even though no validation has been performed, the present study assumes that the behaviour of the physical system is described correctly by the TD model. Full-scale measurements from the Hywind Demo FWT [48] have shown that the tower base bending moment response spectra contain energy around the first tower bending mode and that

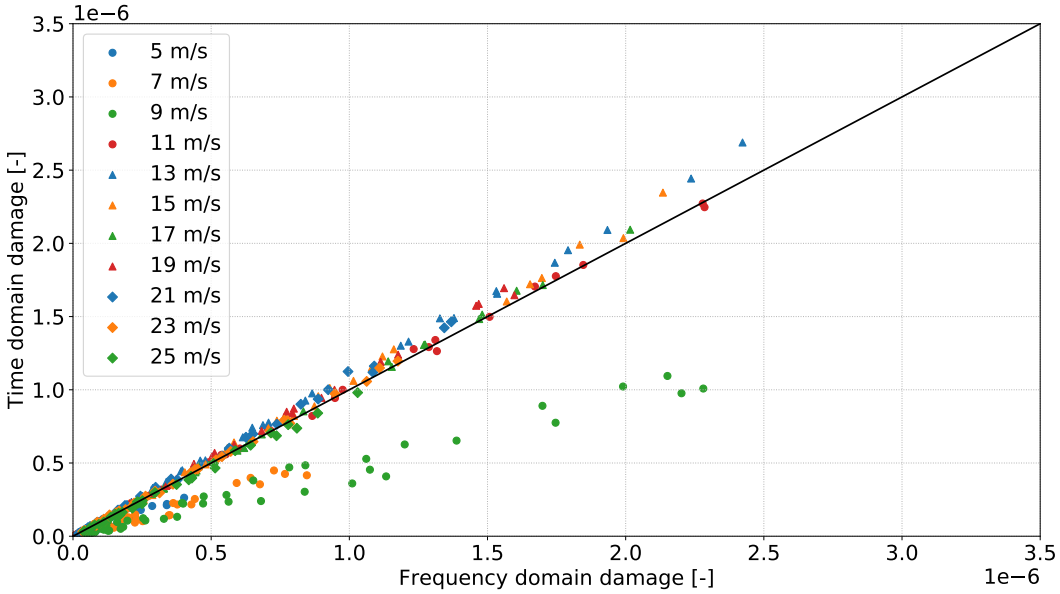

(a) Spar 1.

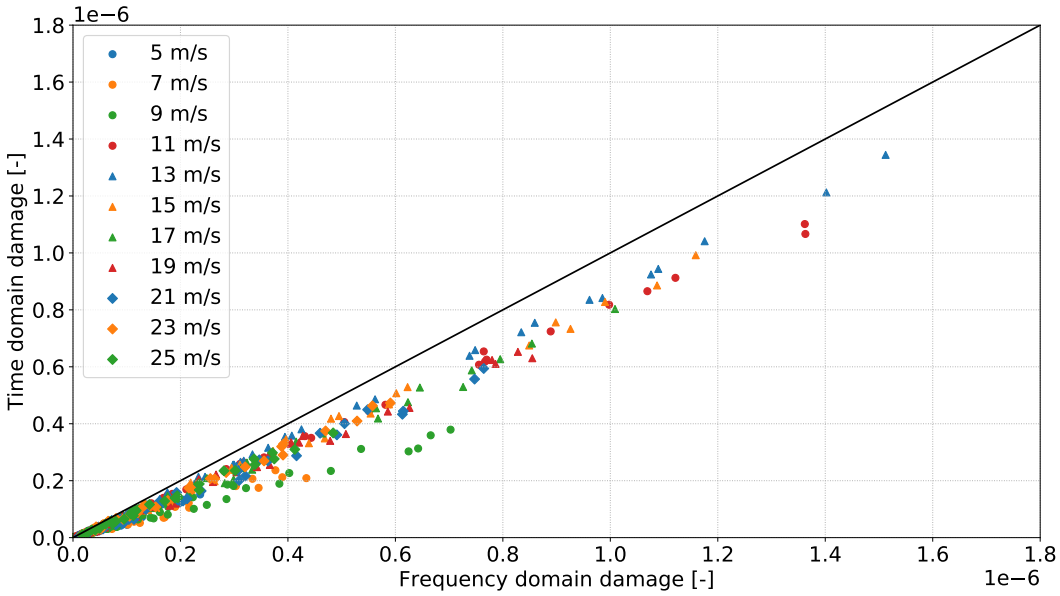

(b) Spar 2.

Figure 9: Time and frequency domain fatigue damage for individual ECs.

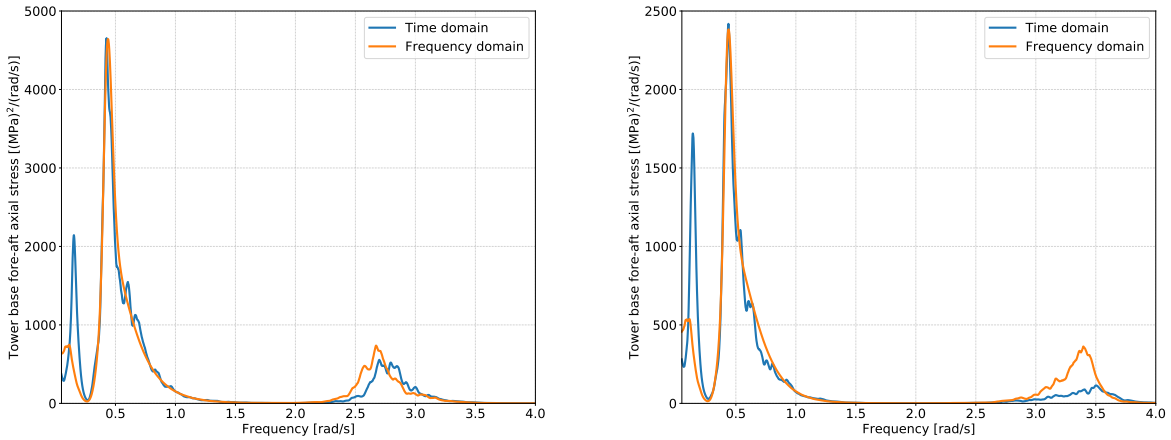

(a) Spar 1 **(b)** Spar 2

Figure 10: Tower base stress response spectrum for $U = 21$ m/s, $H_s = 7.5$ m, $T_p = 14.5$ s.

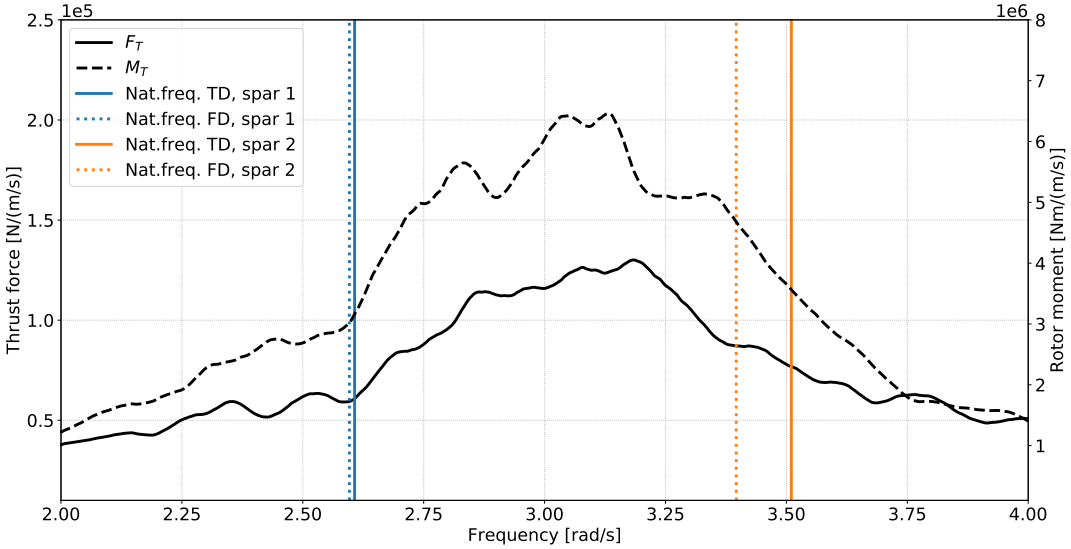

Figure 11: Wind excitation transfer functions around first bending natural frequency, $U = 21$ m/s.

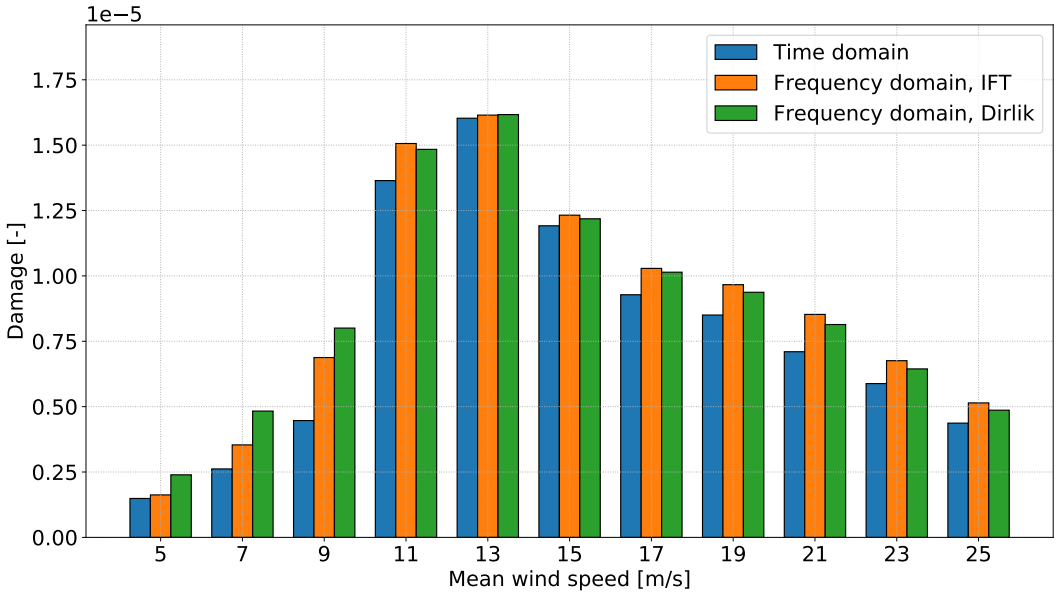

Figure 12: 1-h weighted fatigue damage arranged by wind speed, spar 2 with tuned natural frequency for first bending mode

the numerical models thus capture real effects, however, the actual level of the response is sensitive to the modelling of the system, and may therefore not be correctly represented in the simulations.

6.3 Extreme Value Prediction

The short-term extreme response of the system in the four 50-year environmental conditions is calculated for the tower base bending moment, as well as for the surge and pitch motions of the platform. The results are presented in the following subsections.

6.3.1 Tower Base Bending Moment

Response statistics for the tower base bending moment in the 50-year conditions are listed in Table 6. For a Gaussian process, the skewness is equal to zero, while the Pearson's kurtosis is equal to 3. The skewness and kurtosis values for the tower base bending moment suggest that the responses in EC 2-4 are very close to Gaussian, which is expected, as the bending moments in conditions above cut-out are completely dominated by wave loading, whereas the response in operational conditions with high wind speeds is governed by a combination of wave forces and resonance. The response in EC 1 exhibits some non-Gaussian behaviour due to the large aerodynamic thrust near rated wind speed, however, the degree of nonlinearity is small. In this context, it should also be emphasized that the TD model only includes first order wave loads, with the exception of viscous forces arising from the drag term in Morison's equation.

The standard deviations are accurately predicted by the linear model in all conditions, with relative errors between -2.9% and 4.1%. The mean moments are somewhat less accurate, with the largest errors of 5.5 % (spar 1) and 7.8 % (spar 2) occurring in EC 1, near rated wind speed, where also the largest mean values are found.

Empirical upcrossing rates are plotted together with optimized curve fits and Gaussian upcrossing rates based on the FD results in Figs. 14 and 15. The plots show the multiplication factor κ, which is related to

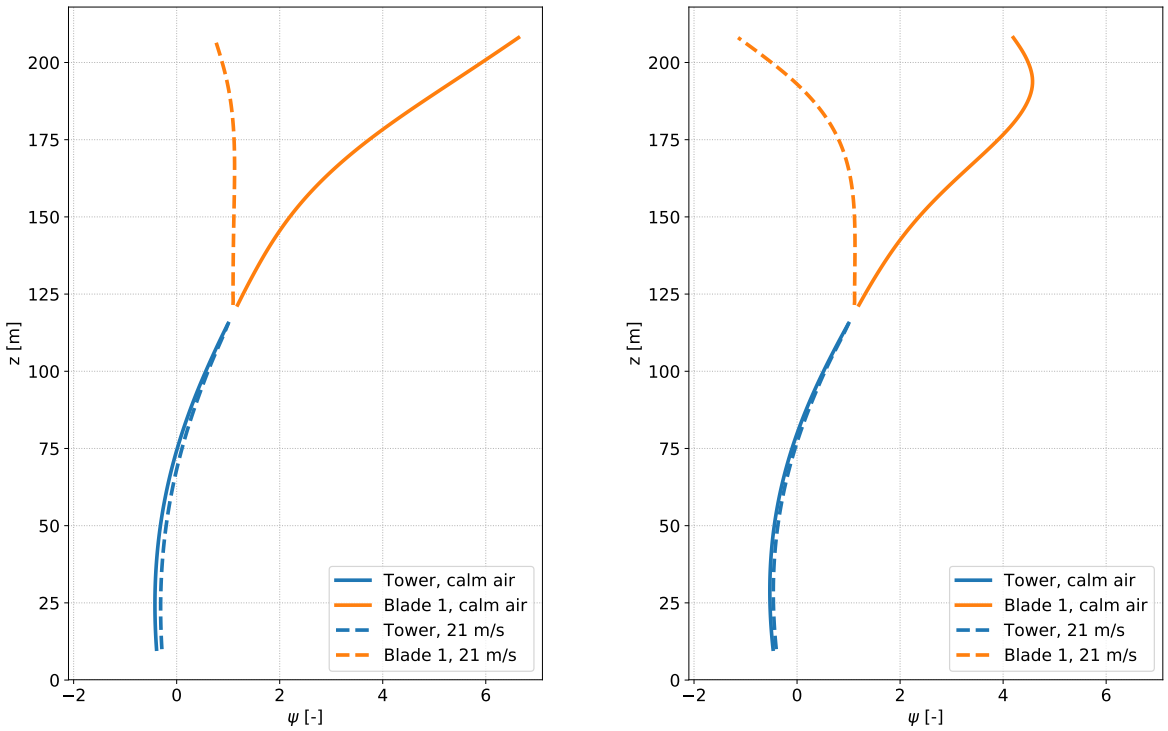

(a) Spar 1 **(b)** Spar 2

Figure 13: Normalized bending mode shapes in calm air and for $U = 21$ m/s. Natural periods found from decay tests are 2.41 s (calm air) and 2.35 s (21 m/s) for spar 1, and 1.79 s (calm air) and 1.75 s (21 m/s) for spar 2.

Table 6: Tower base bending moment statistics, 50-year environmental conditions.

Model	Statistical quantity[1]	Spar 1				Spar 2			
		Condition				Condition			
		1	2	3	4	1	2	3	4
Time domain	Mean (MNm)	247.2	123.0	50.3	105.2	305.7	152.9	63.6	132.8
	Std.dev. (MNm)	89.1	101.0	106.5	118.8	103.8	106.2	115.5	129.7
	Skewness	-0.20	-0.03	-0.01	0.01	-0.30	-0.04	-0.01	0.01
	Kurtosis	3.03	3.00	3.00	3.01	3.13	3.00	3.01	3.01
Frequency domain	Mean (MNm)	260.8	127.8	52.3	101.3	329.4	161.4	66.5	128.9
	Std.dev. (MNm)	89.4	100.8	106.3	115.1	104.8	110.6	118.4	128.5

[1] Time domain results are averaged over 20 seeds.

Table 7: Characteristic largest extreme tower base bending moment y_{1h}, 50-year environmental conditions.

Model	Spar 1				Spar 2			
	Condition				Condition			
	1	2	3	4	1	2	3	4
Time domain (MNm)	534.2	480.6	418.7	509.8	624.1	529.6	462.6	577.4
Frequency domain (MNm)	575.7	491.7	415.4	491.3	699.3	562.0	469.9	563.3
Relative error (%)	7.8	2.3	-0.8	-3.6	12.0	6.1	1.6	-2.4

the extreme response, y, through the relation

$$y = \mu + \kappa\sigma, \tag{28}$$

where μ and σ are the mean and standard deviation of the process. The characteristic largest 1-h extreme for a given environmental condition, which is used in the comparison, corresponds to an upcrossing rate of 2.78×10^{-4}.

The Gaussian upcrossing rates are seen to be conservative for EC 1, due to the slightly nonlinear behaviour which becomes more prominent as the bending moments increase. In the parked conditions, on the other hand, the response is linear also at lower upcrossing rates, and the empirical data are well-described by the linear model.

For spar 1, the FD solution is seen to follow the optimized curve fit closely in EC 2, however, larger discrepancies are observed for spar 2. The fact that the shape of the fitted curve is captured quite well, suggests that the error is related to the overprediction of the bending response discussed in the previous section. As the bending mode is located at a relatively high frequency, the response level has significant influence on the second order spectral moment. Consequently, the mean zero-upcrossing rate (see Eq. (26)) is overestimated by 29% compared to the TD model, which causes a right shift in the linear upcrossing rate curve as observed in Fig. 15b.

The calculated 1-h extreme bending moments are listed in Table 7. The linear estimates give reasonably good approximations of the extreme response, particularly for EC 2-4, as indicated by the upcrossing results.

Due to the high mean value caused by the thrust force, the largest extreme response is found in EC 1. However, this may not be the case in general, and previous studies comparing short-term extremes in selected operational and survival conditions have shown that the largest tower base bending moments for a spar FWT can occur in storm conditions with extreme wind speeds [49, 50]. The critical load cases may vary with floater design and turbine size, as it alters the ratio between wind and wave loads, and for long-term extremes, the probability of the conditions must be taken into account. The most critical operational condition is also not necessarily associated with maximum thrust force on the turbine. In a recent study by Sultania and Manuel [51], the largest 50-year tower base bending moment for a 5 MW spar FWT, considering only operational cases, was found for a mean wind speed of 21.7 m/s. This suggests that a wider range of environmental conditions should be considered in an actual design process.

6.3.2 Global Motions

Tables 8 and 9 list extreme response statistics for surge and pitch, respectively. The global motions show similar behaviour to the tower base bending moments, but as a larger part of the response is located in the low-frequency range, there is less agreement between the TD and FD results for the standard deviations. The values are in general found to be underestimated by the linear model, with errors up to about 20% for both surge and pitch.

As for the bending moments, the upcrossing rates for the global motions (Appendix B) are accurately described by the Gaussian curves in EC 2-4, while the nonlinear behaviour in EC 1 results in conservative

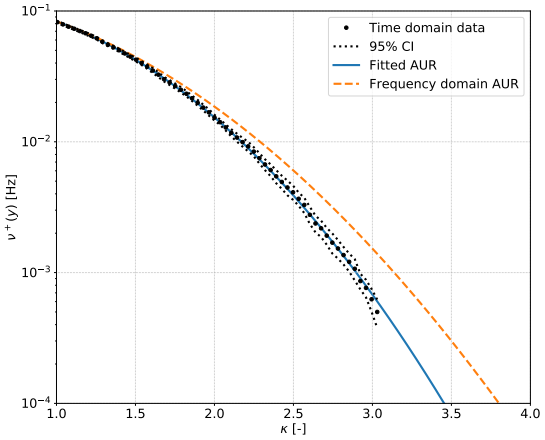

(a) 11 m/s

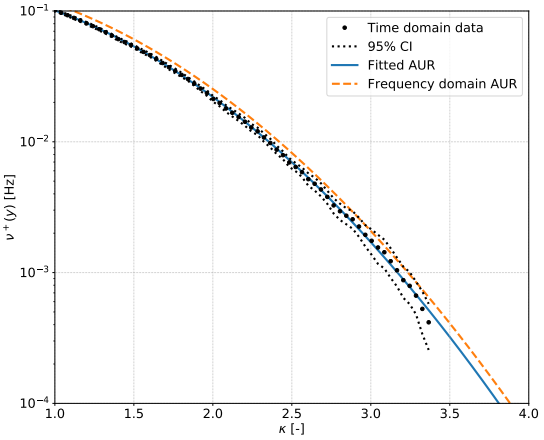

(b) 25 m/s

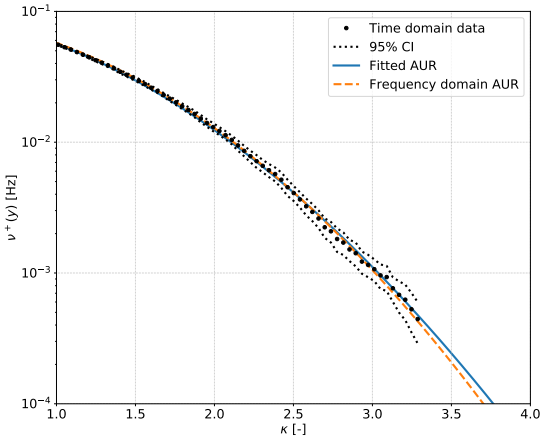

(c) 36 m/s

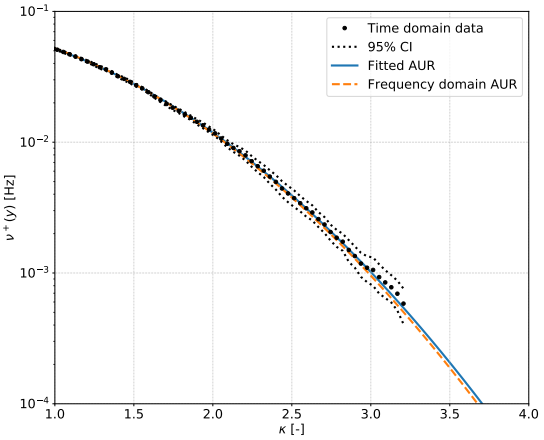

(d) 50 m/s

Figure 14: Tower base bending moment upcrossing rates for spar 1.

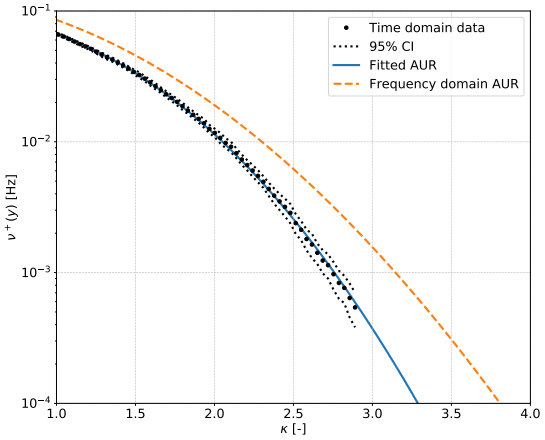

(a) 11 m/s

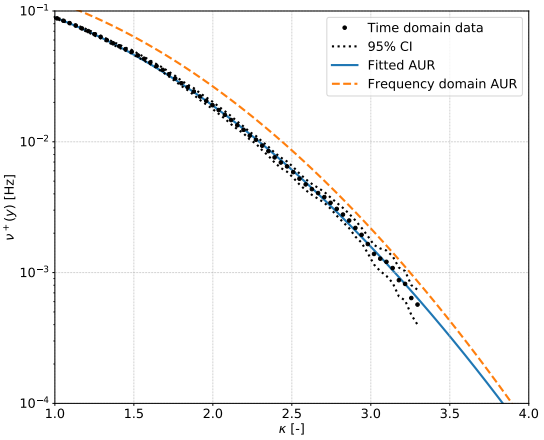

(b) 25 m/s

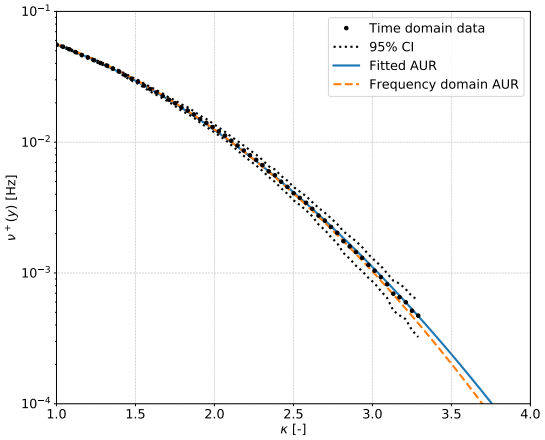

(c) 36 m/s

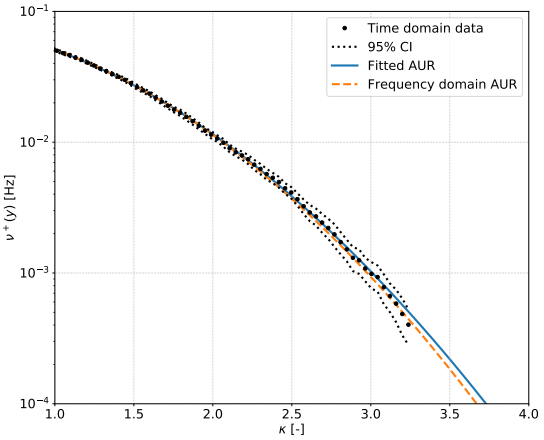

(d) 50 m/s

Figure 15: Tower base bending moment upcrossing rates for spar 2.

Table 8: Platform surge response statistics, 50-year environmental conditions.

Model	Statistical quantity[1]	Spar 1				Spar 2			
		Condition				Condition			
		1	2	3	4	1	2	3	4
Time domain	Mean (m)	27.3	13.8	8.0	15.1	23.7	12.0	6.6	13.7
	Std.dev. (m)	6.9	2.4	2.9	4.6	6.2	2.2	2.7	3.9
	Skewness	-0.14	-0.02	0.05	-0.03	-0.13	-0.01	0.01	0.06
	Kurtosis	2.49	2.90	3.03	3.06	2.57	2.95	3.02	2.97
Frequency domain	Mean (m)	28.6	14.1	7.9	15.3	26.1	12.8	7.0	13.6
	Std.dev. (m)	5.4	2.3	2.5	3.5	5.2	2.2	2.5	3.5

[1] Time domain results are averaged over 20 seeds.

Table 9: Platform pitch response statistics, 50-year environmental conditions.

Model	Statistical quantity[1]	Spar 1				Spar 2			
		Condition				Condition			
		1	2	3	4	1	2	3	4
Time domain	Mean (deg)	6.7	3.4	1.7	3.4	9.2	4.6	2.2	4.4
	Std.dev. (deg)	1.8	1.0	1.2	1.7	2.4	1.3	1.3	2.1
	Skewness	-0.62	0.03	0.04	0.10	-0.72	0.03	0.03	0.10
	Kurtosis	3.37	2.90	3.02	2.99	3.54	2.92	2.99	3.02
Frequency domain	Mean (deg)	7.2	3.5	1.7	3.2	10.0	4.9	2.2	4.3
	Std.dev. (deg)	1.7	1.0	1.0	1.4	2.3	1.2	1.2	1.7

[1] Time domain results are averaged over 20 seeds.

Table 10: Characteristic largest extreme surge response y_{1h}, 50-year environmental conditions.

Model	Spar 1				Spar 2			
	Condition				Condition			
	1	2	3	4	1	2	3	4
Time domain (m)	44.2	21.4	17.8	29.4	38.6	19.0	15.7	26.4
Frequency domain (m)	43.8	21.4	16.1	26.6	40.7	20.0	15.1	24.9
Relative error (%)	-1.0	0.0	-9.5	-9.4	5.4	5.4	-3.6	-5.7

Table 11: Characteristic largest extreme pitch response y_{1h}, 50-year environmental conditions.

Model	Spar 1				Spar 2			
	Condition				Condition			
	1	2	3	4	1	2	3	4
Time domain (deg)	10.7	6.7	5.5	9.1	14.4	8.6	6.6	11.3
Frequency domain (deg)	12.3	6.6	5.0	7.7	16.7	8.7	6.0	9.8
Relative error (%)	14.8	-0.9	-9.4	-14.9	16.2	-4.9	-8.9	-13.2

predictions by the linear model. For both spar designs, some slight nonlinearities are also seen at higher wind speeds, which causes the linear model to underestimate κ at lower upcrossing rates. The discrepancies are likely caused by the aerodynamic drag forces on the tower, which, although they mostly affect the mean position of the FWT, also become more important for the dynamic response as the wind speed increases. The good agreement for the surge motions in the parked conditions suggests that the viscous hydrodynamic forces on the hull contribute little to the motion response.

The resulting characteristic largest 1-h extreme values are listed in Tables 10 and 11. As expected, the most severe global motions are also found in EC 1. The pitch response, which shows the most pronounced non-Gaussian behaviour near rated wind speed, has the least accurate linear predictions in this condition. Large discrepancies are also seen in the most extreme wave condition (EC 4), mostly due to underestimation of the standard deviations in FD. For the surge motions, the extremes found from FD generally agree well with the TD simulations. Most notable are the results in EC 1, especially for spar 1, where the relative error between FD and TD is only -1 %. However, this result is somewhat coincidental, as it is a consequence of the error in κ being almost exactly balanced out by the errors in μ and σ. Nonetheless, the results suggest that the extreme surge motions may be predicted with roughly the same accuracy as the tower base bending moments, despite larger discrepancies in the standard deviations, as the mean values account for a larger share of the total extreme response.

The accuracy of the linear model depends on the importance of nonlinearities in the system, which will vary with location, floater geometry, and different operational conditions. Therefore, the results presented here cannot be generalized to any FWT, and the FD model should be continuously verified against state-of-the-art tools during a design process. The agreement with nonlinear analyses also depends on how the system is represented in the TD model, and care should be taken to make sure that relevant nonlinearities are included.

7 Conclusions

A semi-analytical FD model has been developed, which allows for efficient preliminary design optimization of spar FWTs. The model has been verified against a fully coupled nonlinear TD model for two different 10 MW spar designs, with regards to fatigue damage in the tower base and short-term extreme response in both operational and survival conditions. The fatigue results show that the FD model is accurate in most environmental conditions, especially for spar 1, where the long-term fatigue damage is overestimated by 7%. For spar 2, larger discrepancies are observed, and the linear model overpredicts the damage by approximately 30%. This is found to primarily be caused by errors in the response around the first bending mode, which is highly sensitive to the estimated natural frequency. The accuracy depends on how well the RNA can be approximated as a rigid body for the first bending mode, however, tuning the frequency by adding an artificial stiffness term can be performed in the case where the approximation leads to unacceptable errors.

For 9 m/s mean wind speed, the 3P frequency of the rotor coincides with the natural frequency of the first bending mode for spar 1, which leads to increased damage values and causes the linear model to significantly overpredict the response. The sensitivity with regards to wind speed also suggests that a finer discretization of the wind bins should be applied in a design process, to accurately capture the response around possible resonances. The accuracy of the linear model is found to be fairly independent of wave height and wave period, also for the wind speed which induces 3P resonance with the first tower bending frequency. This indicates that a small number of environmental conditions, which cover the full wind speed range, can be simulated with a TD model to verify and possibly tune the linear model, which then can be used to carry out the full long-term analysis.

The extreme response, both with regards to tower base bending moment and rigid body motions in surge and pitch, is seen to be nearly Gaussian near cut-out and in parked conditions, as it is dominated by wave forces. This results in good agreement for the linear model in these conditions. The largest extremes values are found in EC 1, near rated wind speed, which indicates that a wider range of environmental conditions may be important for the extreme response. The large aerodynamic forces in this condition also introduce some non-Gaussian behaviour, which causes the linear model to overestimate the multiplication factors (κ). However, as the mean values in this condition are relatively large, the inaccuracies in the total extreme response are reduced, and the total error in y_{1h} is within 16% for all considered responses in this condition. Regarding the standard deviations, good agreement between the linear and nonlinear models is obtained for the tower base bending moments, while larger discrepancies are seen for surge and pitch. The reason for this is that the global motions are more dependent on the low-frequency (wind-induced) response, which is less accurately captured by the linear model than the wave- and bending-frequency response. The TD model in the present study only includes first order wave forces, and could thus be improved by also considering higher order loads, which may be important for certain FWT concepts. The model should also be validated through comparisons with physical measurements.

The developed FD model is shown to be well-suited for preliminary design. It gives reasonable agreement with a fully coupled nonlinear TD model, both with regards to fatigue and extreme response, and the semi-analytical approach provides an efficient way to explore the design space. In addition, the closed-form expressions offers the possibility of using analytical gradients in a computer-aided optimization process. However, the efficiency of the model is partly due to the simple geometry of the platform, and the formulations are thus not valid for more complex platform designs, where more comprehensive numerical calculations may be necessary. Also, the approach is only applicable for steady-state conditions, and transient events, which also must be considered, cannot be analysed. Nonetheless, it can serve as a useful complement to more sophisticated models in the design process of spar-type wind turbines, and significantly reduce the needed computational effort.

A Transfer Functions

A.1 Wave Elevation to Tower Base Bending Moment

The transfer function from wave elevation to tower base bending moment is given in Eq. (A.1). The equation considers bending moments due to inertial forces in the tower and RNA, aerodynamic damping forces, and gravitational forces.

$$\begin{aligned} H_{\zeta M}(\omega) = &- \int_{z_{\mathrm{TB}}}^{z_{\mathrm{top}}} m(z)\mathbf{H}_{\zeta\ddot{X}}^{\top}(\omega)\boldsymbol{\psi}(z)(z - z_{\mathrm{TB}})\mathrm{d}z - M_{\mathrm{RNA}}\mathbf{H}_{\zeta\ddot{X}}^{\top}(\omega)\boldsymbol{\psi}(z_{\mathrm{top}})(z_{\mathrm{top}} - z_{\mathrm{TB}}) \\ &- I_{\mathrm{RNA}}\mathbf{H}_{\zeta\ddot{X}}^{\top}(\omega)\boldsymbol{\psi}_{,\boldsymbol{z}}(z_{\mathrm{top}}) - B_{\mathrm{aero}}\mathbf{H}_{\zeta\dot{X}}^{\top}(\omega)\boldsymbol{\psi}(z_{\mathrm{top}})(z_{\mathrm{top}} - z_{\mathrm{TB}}) \\ &+ \int_{z_{\mathrm{TB}}}^{z_{\mathrm{top}}} m(z)g\mathbf{H}_{\zeta X}^{\top}(\omega)\left[\boldsymbol{\psi}(z) - \boldsymbol{\psi}(z_{\mathrm{TB}})\right]\mathrm{d}z + M_{\mathrm{RNA}}g\mathbf{H}_{\zeta X}^{\top}(\omega)\left[\boldsymbol{\psi}(z_{\mathrm{top}}) - \boldsymbol{\psi}(z_{\mathrm{TB}})\right] \end{aligned} \tag{A.1}$$

A.2 Wind Speed to Tower Base Bending Moment

The transfer function from wind speed to tower base bending moment is given in Eq. (A.2). The equation considers bending moments due to inertial forces in the tower and RNA, aerodynamic damping forces, gravitational forces, and wind excitation forces.

$$\begin{aligned} H_{UM}(\omega) = &- \int_{z_{\mathrm{TB}}}^{z_{\mathrm{top}}} m(z)\mathbf{H}_{U\ddot{X}}^{\top}(\omega)\boldsymbol{\psi}(z)(z - z_{\mathrm{TB}})\mathrm{d}z - M_{\mathrm{RNA}}\mathbf{H}_{U\ddot{X}}^{\top}(\omega)\boldsymbol{\psi}(z_{\mathrm{top}})(z_{\mathrm{top}} - z_{\mathrm{TB}}) \\ &- I_{\mathrm{RNA}}\mathbf{H}_{U\ddot{X}}^{\top}(\omega)\boldsymbol{\psi}_{,\boldsymbol{z}}(z_{\mathrm{top}}) - B_{\mathrm{aero}}\mathbf{H}_{\zeta\dot{X}}^{\top}(\omega)\boldsymbol{\psi}(z_{\mathrm{top}})(z_{\mathrm{top}} - z_{\mathrm{TB}}) \\ &+ \int_{z_{\mathrm{TB}}}^{z_{\mathrm{top}}} m(z)g\mathbf{H}_{UX}^{\top}(\omega)\left[\boldsymbol{\psi}(z) - \boldsymbol{\psi}(z_{\mathrm{TB}})\right]\mathrm{d}z + M_{\mathrm{RNA}}g\mathbf{H}_{UX}^{\top}(\omega)\left[\boldsymbol{\psi}(z_{\mathrm{top}}) - \boldsymbol{\psi}(z_{\mathrm{TB}})\right] \\ &+ F_T(\omega)(z_{\mathrm{top}} - z_{\mathrm{TB}}) + M_T(\omega) \end{aligned} \tag{A.2}$$

B Upcrossing Rates for Global Motions

B.1 Surge

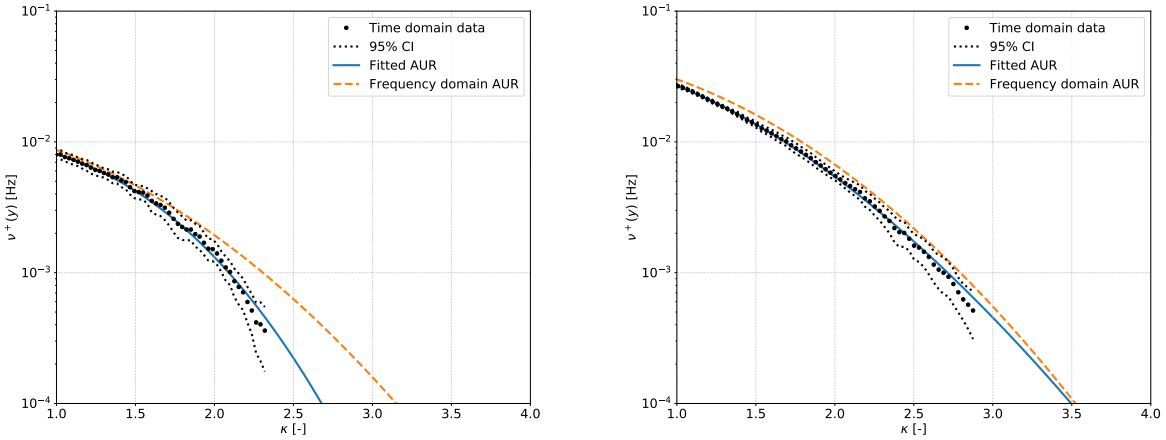

(a) 11 m/s

(b) 25 m/s

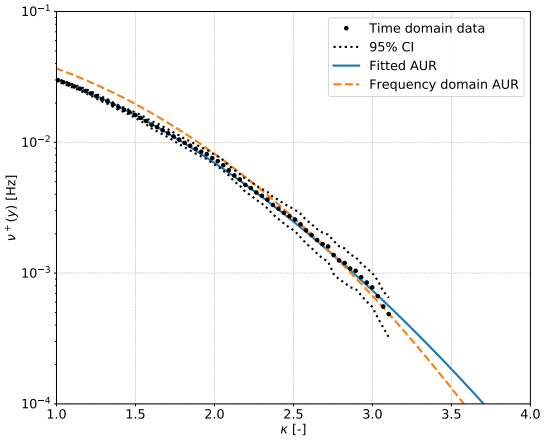

(c) 36 m/s

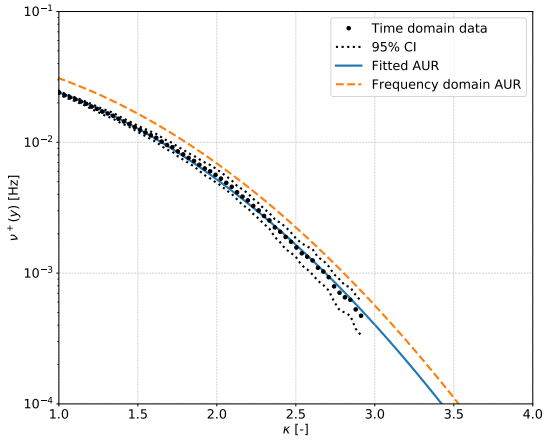

(d) 50 m/s

Figure B.1: Platform surge upcrossing rates for spar 1.

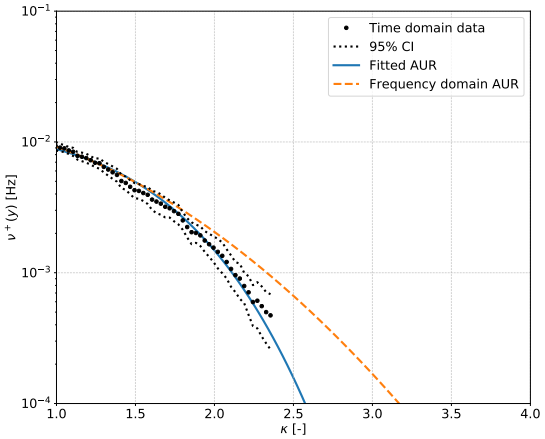

(a) 11 m/s

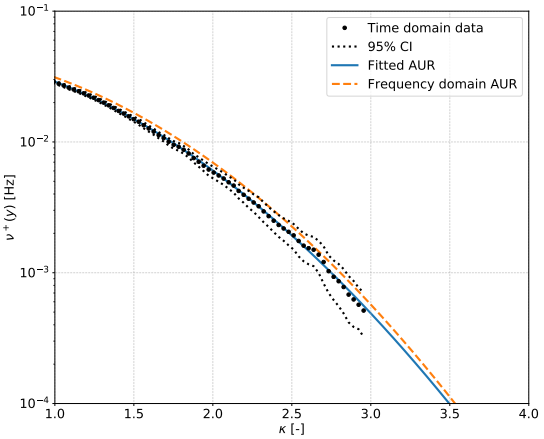

(b) 25 m/s

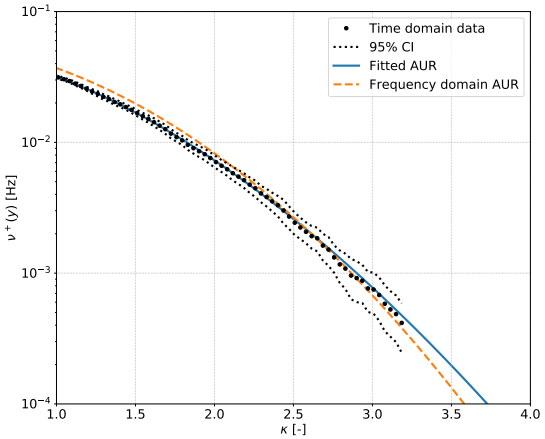

(c) 36 m/s

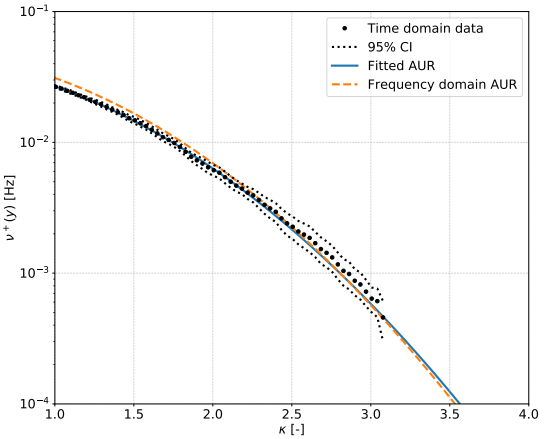

(d) 50 m/s

Figure B.2: Platform surge upcrossing rates for spar 2.

B.2 Pitch

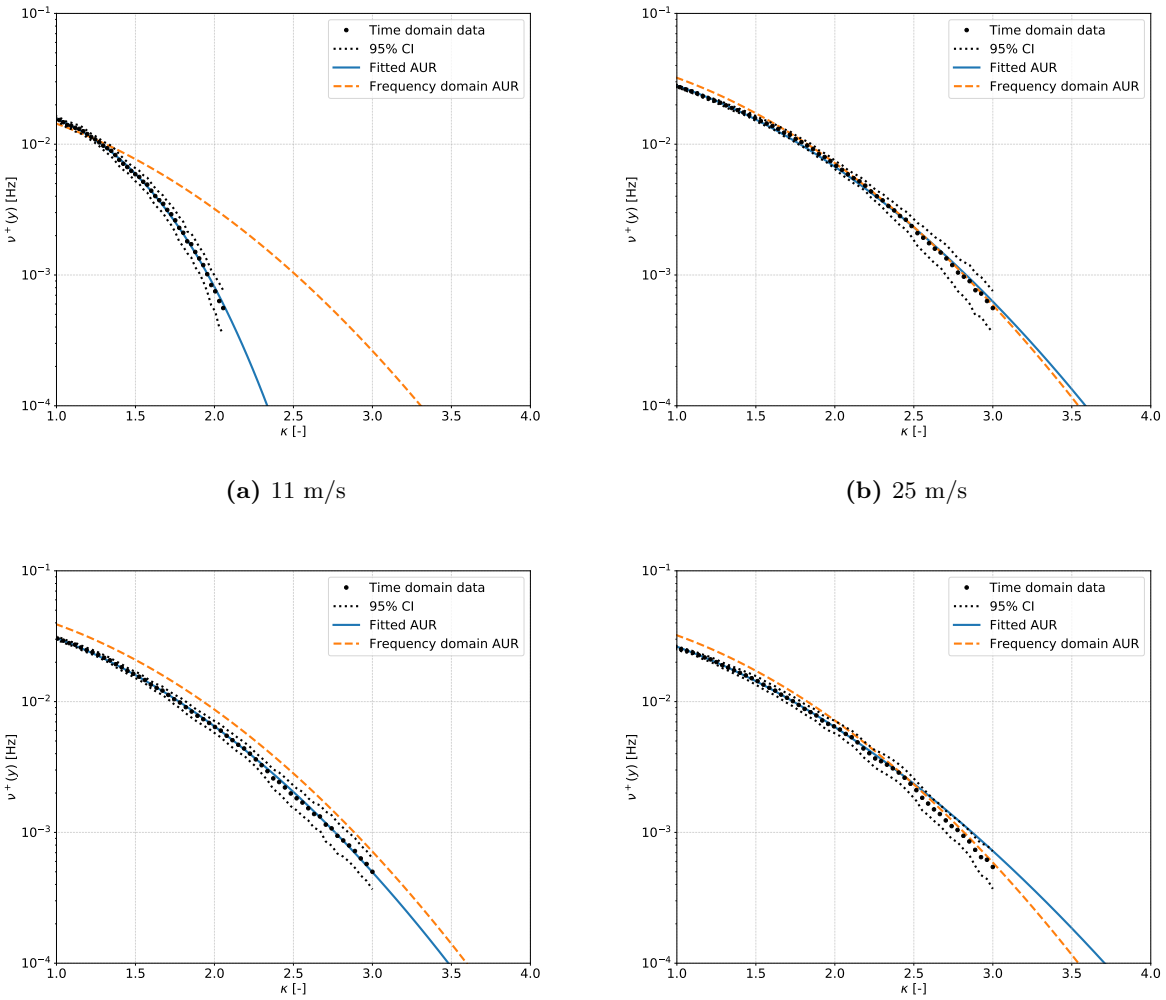

(a) 11 m/s

(b) 25 m/s

(c) 36 m/s

(d) 50 m/s

Figure B.3: Platform pitch upcrossing rates for spar 1.

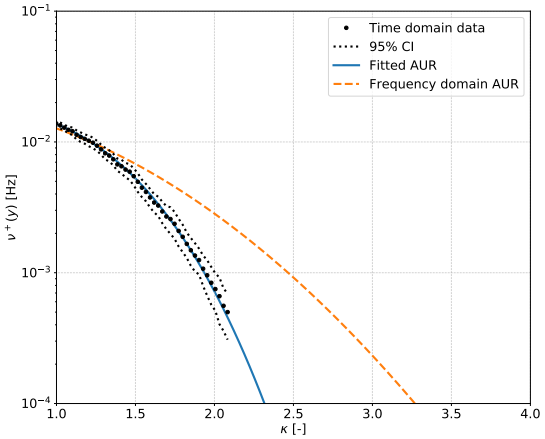

(a) 11 m/s

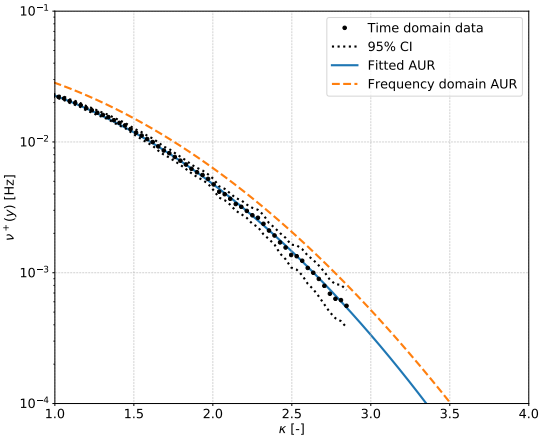

(b) 25 m/s

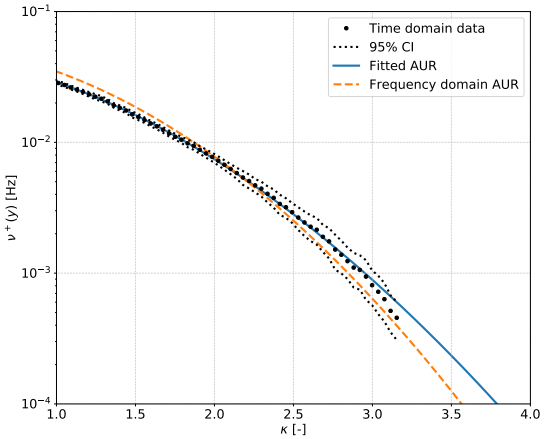

(c) 36 m/s

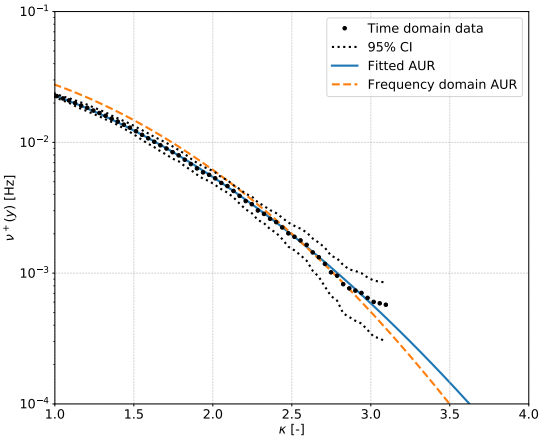

(d) 50 m/s

Figure B.4: Platform pitch upcrossing rates for spar 2.

References

[1] M. Strach-Sonsalla and M. Muskulus. "Dynamics and Design of Floating Wind Turbines". In: *Proceedings of the Twenty-sixth (2016) International Ocean and Polar Engineering Conference (ISOPE2016), Rhodes, Greece*. 2016.

[2] DNV. *Environmental Conditions and Environmental Loads*. Tech. rep. DNV-RP-C205. 2014.

[3] DNV. *Design of Floating Wind Turbine Structures*. Tech. rep. OS-J103. 2013.

[4] E. N. Wayman et al. "Coupled Dynamic Modeling of Floating Wind Turbine Systems". In: *Offshore Technology Conference*. 2006.

[5] P. Sclavounos, C. Tracy, and S. Lee. "Floating Offshore Wind Turbines: Responses in a Seastate Pareto Optimal Designs and Economic Assessment". In: *Proceedings of the ASME 27th International Conference on Offshore Mechanics and Arctic Engineering (OMAE2008), Estoril, Portugal*. 2008.

[6] M. Philippe, A. Babarit, and P. Ferrant. "Comparison of Time and Frequency Domain Simulations of an Offshore Floating Wind Turbine". In: *Proceedings of the ASME 2011 30th International Conference on Ocean, Offshore and Arctic Engineering (OMAE2011), Rotterdam, The Netherlands*. 2011.

[7] K. Wang et al. "Frequency Domain Approach for the Coupled Analysis of Floating Wind Turbine System". In: *Ships and Offshore Structures* 12.6 (2017), pp. 767–774.

[8] E. E. Bachynski and T. Moan. "Linear and Nonlinear Analysis of Tension Leg Platform Wind Turbines". In: *Proceedings of the Twenty-second (2012) International Offshore and Polar Engineering Conference (ISOPE2012), Rhodes, Greece*. 2012.

[9] E. E. Bachynski. "Design and Dynamic Analysis of Tension Leg Platform Wind Turbines". PhD thesis. Norwegian University of Science and Technology, 2014.

[10] M. I. Kvittem and T. Moan. "Frequency Versus Time Domain Fatigue Analysis of a Semisubmersible Wind Turbine Tower". In: *Journal of Offshore Mechanics and Arctic Engineering* 137.1 (2014).

[11] J. M. Kluger, T. P. Sapsis, and A. H. Slocum. "A Reduced-Order, Statistical Linearization Approach For Estimating Nonlinear Floating Wind Turbine Response Statistics". In: *Proceedings of the Twenty-sixth (2016) International Ocean and Polar Engineering Conference (ISOPE2016), Rhodes, Greece*. 2016.

[12] J. Jonkman. *Definition of the Floating System for Phase IV of OC3*. Tech. rep. NREL/TP-500-47535. National Renewable Energy Laboratory, 2010.

[13] D. Matha. "Model Development and Loads Analysis of an Offshore Wind Turbine on a Tension Leg Platform, with a Comparison to Other Floating Turbine Concepts". MA thesis. University of Colorado - Boulder, 2009.

[14] M. Karimirad and T. Moan. "Extreme Dynamic Structural Response Analysis of Catenary Moored Spar Wind Turbine in Harsh Environmental Conditions". In: *Journal of Offshore Mechanics and Arctic Engineering* 133 (2011).

[15] N. Aggarwal, R. Manikandan, and N. Saha. "Nonlinear short term extreme response of spar type floating offshore wind turbines". In: *Ocean Engineering* 130 (2017), pp. 199–209.

[16] C. Bak et al. *Description of the DTU 10 MW Reference Wind Turbine*. Tech. rep. DTU Wind Energy Report-I-0092. DTU Wind Energy, 2013.

[17] MARINTEK. *RIFLEX User Guide*. 2016.

[18] MARINTEK. *SIMO User Guide*. 2016.

[19] Wamit Inc . *WAMIT User Manual*. 2014.

[20] L. Roald et al. "The effect of second-order hydrodynamics on floating offshore wind turbines". In: *Energy Procedia* 35 (2013), pp. 253–264.

[21] T. Duarte, A. J. Sarmento, and J. Jonkman. "Effects of Second-Order Hydrodynamic Forces on Floating Offshore Wind Turbines". In: *32nd ASME Wind Energy Symposium, National Harbor, Maryland*. 2014.

[22] H. Ormberg and E. E. Bachynski. "Global Analysis of Floating Wind Turbines: Code Development, Model Sensitivity and Benchmark Study". In: *Proceedings of the Twenty-second (2012) International Offshore and Polar Engineering Conference (ISOPE2012), Rhodes, Greece*. 2012.

[23] A. Robertson et al. "Offshore Code Comparison Collaboration Continuation within IEA Wind Task 30: Phase II Results Regarding a Floating Semisubmersible Wind System". In: *Proceedings of the ASME 2014 33rd International Conference on Ocean, Offshore and Arctic Engineering (OMAE2014), San Francisco, California, USA*. 2014.

[24] F. G. Nielsen, T. D. Hanson, and B. Skaare. "Integrated Dynamic Analysis of Floating Offshore Wind Turbines". In: *Proceedings of OMAE 2006 25th International Conference on Offshore Mechanics and Arctic Engineering, Hamburg, Germany*. 2006.

[25] T. J. Larsen and T. D. Hanson. "A Method to Avoid Negative Damped Low Frequent Tower Vibrations for a Floating, Pitch Controlled Wind Turbine". In: *Journal of Physics: Conference Series* 75 (2007), p. 012073.

[26] A. Naess and T. Moan. *Stochastic Dynamics of Marine Structures*. Cambridge University Press, 2013.

[27] J. N. Newman. *Marine Hydrodynamics*. The MIT Press, 1977.

[28] R. C. MacCamy and R. A. Fuchs. *Wave Forces on Piles: a Diffraction Theory*. Tech. rep. Technical Memorandum 69. Beach Erosion Board; Corps of Engineers, 1954.

[29] J. van der Tempel. "Design of Support Structures for Offshore Wind Turbines". PhD thesis. TU Delft, 2006.

[30] D. J. C. Salzmann and J. van der Tempel. "Aerodynamic Damping in the Design of Support Structures for Offshore Wind Turbines". In: *Proceedings of the Offshore Wind Energy Conference, Copenhagen, Denmark*. 2005.

[31] L. E. Borgman. "Ocean Wave Simulation for Engineering Design". In: *Journal of the Waterways and Harbors Division* 95.4 (1969), pp. 557–586.

[32] O. M. Faltinsen. *Sea Loads on Ships and Offshore Structures*. Cambridge University Press, 1990.

[33] K. Johannessen, T. S. Meling, and S. Haver. "Joint Distribution for Wind and Waves in the Northern North Sea". In: *International Journal of Offshore and Polar Engineering* 12.1 (2002), pp. 1–8.

[34] IEC. *Design Requirements for Offshore Wind Turbines*. Tech. rep. IEC 61400-3. 2009.

[35] M. I. Kvittem and T. Moan. "Time Domain Analysis Procedures for Fatigue Assessment of a Semi-Submersible Wind Turbine". In: *Marine Structures* 40 (2015), pp. 38–59.

[36] B. J. Jonkman and L. Kilcher. *TurbSim User's Guide: Version 1.50*. Tech. rep. NREL/TP-500-46198. National Renewable Energy Laboratory, 2009.

[37] E. E. Bachynski et al. "Dynamic analysis of floating wind turbines during pitch actuator fault, grid loss, and shutdown". In: *Energy Procedia* 35 (2013), pp. 210–222.

[38] Z. Jiang, M. Karimirad, and T. Moan. "Dynamic response analysis of wind turbines under blade pitch system fault, grid loss, and shutdown events". In: *Wind Energy* 17 (2014), pp. 1385–1409.

[39] T. Dirlik. "Application of Computers in Fatigue Analysis". PhD thesis. University of Warwick, 1985.

[40] Z. Gao and T. Moan. "Frequency-domain fatigue analysis of wide-band stationary Gaussian processes using a trimodal spectral formulation". In: *International Journal of Fatigue* 30.10-11 (2008), pp. 1944–1955.

[41] P. Ragan and L. Manuel. "Comparing Estimates of Wind Turbine Fatigue Loads using Time-Domain and Spectral Methods". In: *Wind Engineering* 31.2 (2007), pp. 83–99.

[42] DNV. *Fatigue Design of Offshore Steel Structures*. Tech. rep. DNV-RP-C203. 2010.

[43] N. Aggarwal, R. Manikandan, and N. Saha. "Predicting Short Term Extreme Response of Spar Offshore Floating Wind Turbine". In: *Procedia Engineering* 116.1 (2015), pp. 47–55.

[44] A. Naess and O. Gaidai. "Monte Carlo Methods for Estimating the Extreme Response of Dynamical Systems". In: *Journal of Engineering Mechanics* 134.8 (2008), pp. 628–636.

[45] N. Saha et al. "Short-Term Extreme Response Analysis of a Jacket Supporting an Offshore Wind Turbine". In: *Wind Energy* 17 (2014), pp. 87–104.

[46] N. Saha and A. Naess. "Monte Carlo-Based Method for Predicting Extreme Value Statistics of Uncertain Structures". In: *Journal of Engineering Mechanics* 136.12 (2010), pp. 1491–1501.

[47] M. I. Kvittem et al. "Short-Term Fatigue Analysis of Semi-Submersible Wind Turbine Tower". In: *Proceedings of the ASME 2011 30th International Conference on Ocean, Offshore and Arctic Engineering (OMAE2011), Rotterdam, The Netherlands*. 2011.

[48] B. Skaare et al. "Analysis of measurements and simulations from the Hywind Demo floating wind turbine". In: *Wind Energy* 18 (2015), pp. 1105–1122.

[49] M. Karimirad and T. Moan. "Wave- and Wind-Induced Dynamic Response of a Spar-Type Offshore Wind Turbine". In: *Journal of Waterway, Port, Coastal, and Ocean Engineering* 138.1 (2012), pp. 9–20.

[50] M. J. Muliawan et al. "Extreme responses of a combined spar-type floating wind turbine and floating wave energy converter (STC) system with survival modes". In: *Ocean Engineering* 65 (2013), pp. 71–82.

[51] A. Sultania and L. Manuel. "Reliability analysis for a spar-supported floating offshore wind turbine". In: *Wind Engineering* 42.1 (2018), pp. 51–65.